

Chapter 6

Alternative Electrodes for OSC

Yong Zhang and Bryce Nelson

6.1 Introduction

Transparent conductive electrodes (TCEs) are essential components of many ubiquitous commercial optoelectronic devices such as solar cells [1], liquid-crystal displays (LCDs) [2], light-emitting diodes (LEDs) [3], touch screens [4], electrochromic windows [5] and thin-film transistors (TFTs) [6]. Doped metal oxide-coated glasses, such as indium tin oxide (ITO), fluorine tin oxide (FTO) [7] and aluminium zinc oxide (AZO) [8, 9], are currently the most common material-of-choice for TCEs. However, the scarcity of the rare-earth metal indium and the high market demand for TCEs have resulted in future supply concerns, increasing cost, and price fluctuation. It has been reported that while the global demand for resistive style touch panels has recently grown at ~30 % per year, the world-wide production of indium, a critical component, increased by only 5 % annually between 2000 and 2010 [10]. As a result, the price of indium in the USA has increased by approximately 6–10 times during this time. In addition to supply and price constraints, the processing of ITO requires a number of energy intensive processes such as high preparation temperatures and vacuum-based deposition techniques. The brittleness of ITO and its substitutes FTO and AZO make it unsuitable for use in flexible and stretchable electronic devices [11, 12]. Unless these issues are addressed, the high cost and limitations of ITO and its current substitutes are expected to slow both innovation and adoption of optoelectronic device technology.

Over the last two decades, the field of organic and hybrid solar cells has touted ever-increasing power conversion efficiencies (PCEs), with several numerous publications featuring devices that achieve over 10 % PCE, long a benchmark of market-leading thin film inorganic-based solar technologies [13, 14]. With com-

Y. Zhang (✉) · B. Nelson
Sigma-Aldrich Corporation, Materials Science,
6000 N Teutonia Ave., Milwaukee, WI 53209, USA
e-mail: yong.zhang@sial.com

B. Nelson
e-mail: bryce.nelson@sial.com

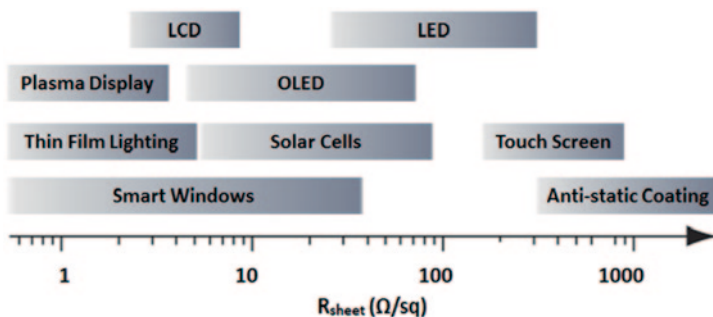


Fig. 6.1 The range of sheet resistance requirements of different optoelectronic devices

mercialization on the horizon, the emphasis has moved towards translating laboratory progress into cost-effective, production-ready modules. Because ITO accounts for more than half of the total cost of organic photovoltaic modules [15, 16], it is believed that identifying an alternative electrode material to replace ITO is essential to enable this disruptive technology. While, low-cost, high-throughput roll-to-roll (R2R) printing technology is envisioned by many to be critical to any successful manufacturing approach [17], the basic requirements for a successful alternative electrode material are relatively simple: plentiful and affordable raw materials, compatible with low cost processing, as well as flexible and/or stretchable.

The materials that have emerged for use in alternative electrodes can be classified into three major categories: (1) inorganic nanomaterials including metal [18–22] or metal oxides [8, 9] (since doped metal oxides have no advantage to ITO in terms of processing, it will not be discussed in this chapter); (2) organic materials including polymers [23, 24], carbon nanotubes (CNTs) [25–27] and graphene [28–30]; (3) hybrid materials, including multiple components of (1) and (2) [31, 32].

High electrical conductivity and optical transparency are the essential performance parameters for a TCE. These parameters are largely governed by the film thickness and are typically in opposition to each other. Commercially available ITO-based TCEs have relatively high conductivity (sheet resistance of 10–20 Ω/sq) and transmission (>90%) in the visible region of the solar spectrum. While it is generally accepted that any alternative to ITO must have a sheet resistance of at least $R_s < 100 \Omega/\text{sq}$ coupled with transmittance $T > 80\%$ in the visible range [33], each application has its own unique requirements. Large-area display, including plasma display and solid-state thin film lighting, will require even lower sheet resistance $< 5 \Omega/\text{sq}$ [34]. Figure 6.1 illustrates the range of sheet resistance requirements for various optoelectronic devices.

The intrinsic properties of the TCE components will ultimately limit the overall performance of a TCE [35]. To achieve a high DC conductivity σ_{DC} , a material must have either a high concentration of carriers (either n (electrons) or p (holes)), or a high carrier mobility $\mu_{n,p}$, given as

$$\sigma_{\text{DC}} = en\mu_{n,p} \quad (6.1)$$

where e is the elementary charge. However, on the optical side, the optical transmission is limited by free carriers (electrons). In an electromagnetic field, the carrier gas (electrons) forms a collective plasma excitation in a conductor. Classical Drude theory gives the plasma frequency as:

$$\omega_p = \sqrt{\frac{ne^2}{m^* \epsilon_r \epsilon_0}} \quad (6.2)$$

where m^* is the effective mass of the carriers and $\epsilon_r \epsilon_0$ is the permittivity of the conductor. The plasma wavelength is given as:

$$\lambda_p = 2\pi\hbar / \omega_p \quad (6.3)$$

which is the material's cutoff wavelength of the optical transmittance spectrum. If the wavelength is above the plasma wavelength ($> \lambda_p$), the light is reflected; if below ($< \lambda_p$), the light is transmitted. Thus with a high concentration of free electrons (n) resulting a low cutoff plasma wavelength λ_p , metals ($n \gg 10^{22} \text{ cm}^{-3}$) and semiconductors ($n \approx 10^{21} \text{ cm}^{-3}$) are usually opaque in the deep-ultraviolet and visible range.

Based on the fundamental equations above, it can be concluded that, as a general rule, the best TCE materials combine low carrier concentration (n or p) and high carrier mobility ($\mu_{n,p}$). For applications such as displays (e.g. LCD or LED), transparency in the visible region only is sufficient. However, communication and photovoltaic applications require use of narrow-bandgap semiconductors and TCE transparency in the infrared (IR) spectrum, where ITO has significant reflectance.

Besides the carrier concentration n and carrier mobility μ , film thickness t is the other major determinant of (R_s , T) in a TCE. Some researchers now report an intrinsic measurement, called as figure-of-merit (FOM) [33, 36], to enable a direct and accurate comparison of different materials at various thicknesses. Since the sheet resistance of a conducting film is indeed physically linked with its transparency, the sheet resistance is then determined by DC conductivity σ_{DC} .

$$R_s = \frac{1}{\sigma_{DC} t} \quad (6.4)$$

And the transmittance is controlled by optical conductivity σ_{OP} by

$$T = \left(1 + \frac{Z_o}{2} \sigma_{OP} t \right)^{-2} \quad (6.5)$$

where $Z_0 = 377 \Omega$ is the impedance of free space. A combination of Eqs. (6.4) and (6.5) can eliminate the film thickness t and gives

$$T = \left(1 + \frac{Z_o}{2R_s} \frac{\sigma_{OP}}{\sigma_{DC}} \right)^{-2} \quad (6.6)$$

The (R_s, T) pair is therefore only determined by the conductivity ratio (Eq. 6.6).

$$\text{FOM} = \frac{\sigma_{\text{DC}}}{\sigma_{\text{OP}}} = \frac{Z_o}{2 \left(\frac{1}{\sqrt{T}} - 1 \right) R_s} \quad (6.7)$$

A high FOM indicates a TCE with a high T at a low R_s . The minimum industrial requirement ($100 \text{ } \Omega/\text{sq}$, $T=80\%$) can now be translated into $\text{FOM} > 16$ using Eq. 6.7. Although the FOM is a semi-empirical approach (T at 550 nm and neglecting the substrate contribution), it offers sufficiently high accuracy and facilitates the comparison among various TCEs. For example, the FOM for commercially available ITO sheets (e.g. Aldrich Prod No.703192: $8\text{--}60 \text{ } \Omega/\text{sq}$, $T=84\%$) generally fall into the range $35\text{--}260$ [37]. Well-doped graphene can possess $R_s = 62.4/N \text{ } \Omega/\text{sq}$ for $T=100\text{--}2.3 \text{ N } (\%)$ varying with the number of layers N [38], resulting in an FOM ranging from 244 (four-layer) to 258 (single-layer).

In this chapter, a brief summary of recent research on alternative TCEs is provided with references to important publications. In addition, several commercialized products are highlighted for perspective on the requirements for real-world industrial solar cell application.

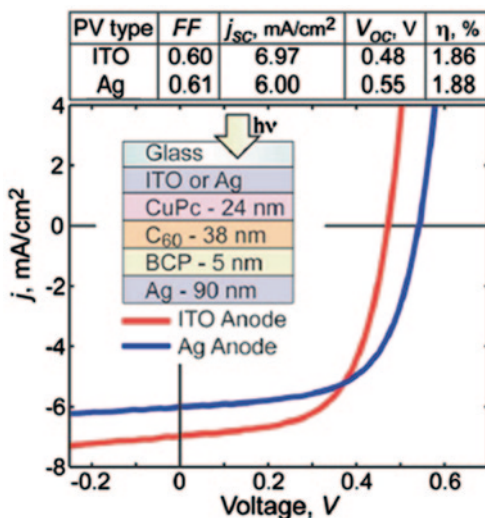
6.2 Inorganic Nanomaterial-Based Alternative TCEs

Although metals with a relatively high concentration of free electrons ($n \gg 10^{22} \text{ cm}^{-3}$) are usually opaque in the deep-ultraviolet and visible range, very thin evaporated metals are semi-transparent and were once used as conductive electrodes in early optoelectronics. However, the use of these thin semi-transparent metals rapidly declined after ITO emerged as the dominant material of choice for TCEs. Ironically, researchers are now revisiting the use of transparent metals due to the high cost and inflexibility of ITO. It is especially noted that some metals, such as silver and gold are highly suited for flexible electronics because of their high thermo-mechanical robustness in comparison to ITO. The brittle nature of ITO limits both the amount of thermo-mechanical load it can withstand as well as its small bend radii. Under a relatively low load, ITO will degrade and crack. Silver, however, is less brittle and can withstand both moderate thermo-mechanical loading and small bend radii. For these reasons, thin metal layers, metal nano grids and nanowires are now under investigation as potential ITO replacements.

6.2.1 Thin Metal Layers

When using a thin metal film to replace ITO, film thickness is a critical parameter that must be carefully adjusted to balance conductivity and transparency. As men-

Fig. 6.2 The J - V characteristics for 1 mm diameter, ITO and Ag anode-based OPV cells under 106 mW/cm^2 illumination. The ITO thickness is 150 nm and the semi-transparent Ag electrode is 9 nm. Relevant device performance parameters are summarized in the table. Inset: The layer structure of the organic solar cells. (Reprinted with permission from Ref. [41])



tioned in the introduction, the surface scattering of free charge carriers in thin metal films causes an inverse relationship between film resistivity and thickness (Eq. 6.4). Achieving low sheet resistance is important for OPV cell scale up in order to reduce loss while transporting charge to external circuitry. On the other hand, optical transmission follows the Beer–Lambert law such that an increasing thickness results in decreasing transmission. Thus, there is an inverse relationship between transmission and sheet resistance as well: thinner electrode films generally exhibit higher resistivity due to electron scattering from the surface as well as from grain boundaries. Amongst the commonly used metal conductors, such as Al, Au [39], Ag and Ti [9], Ag has the best combination of optical properties, lowest sheet resistance (down to $1.6 \times 10^{-6} \Omega \text{ cm}$), good stability and high corrosion resistance. Mapel et al. [40] demonstrated that when used as an anode material, Ag forms an ohmic contact with the photoactive materials in an OPV device. O'Connor et al. compared the device performance of a small molecule OPV device using semi-transparent thin Ag electrodes with those using ITO. The theoretical Fuchs–Sondheimer (FS)–Mayadas–Shatzkes (MS) model suggests that thin Ag films can replace or even outperform ITO in bulk heterojunction (BHJ) OPV cells, without further texturing or nano/micropatterning of the electrode as shown in Fig. 6.2 [41]. Experimental results verify the effect of the thickness of Ag layer on the J_{sc} , V_{OC} and fill factor (FF): J_{sc} is strongly dependent on thickness due to the in-coupling of light through the transparent metal conductor film, while V_{OC} and FF are affected much less.

Thermal evaporation is the most common method for the deposition of thin metal films. However, the high cost associated with the thermal evaporation equipment and batch process makes it incompatible with the fabrication of low cost organic and hybrid solar cells. Further, the tendency of metals to coalesce and interfere with film formation when deposited onto organic layers complicates this approach [21]. Recently, a thin film Ag/ZnO electrode was used in the fabrication of large

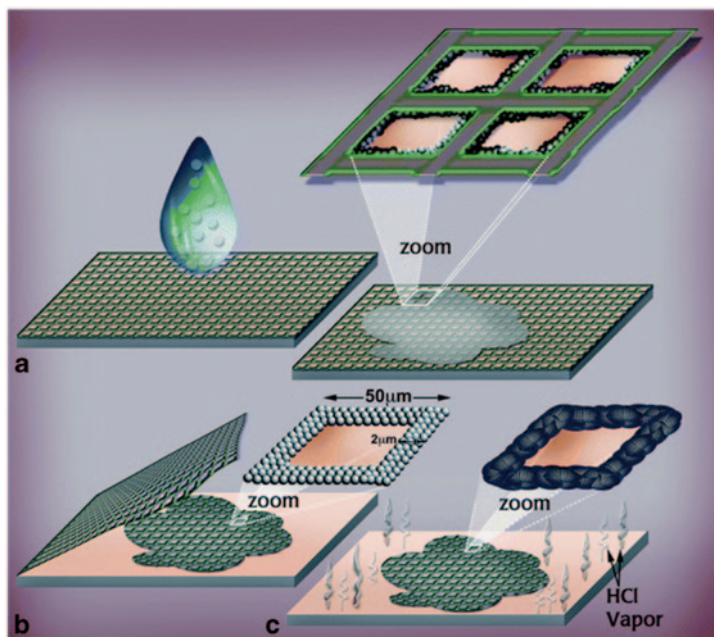


Fig. 6.3 Schematic presentation of the fabrication process to obtain a transparent and conductive metallic grid. (Reprinted with permission from Ref. [47])

area OPV modules using all-solution-based R2R processing. The resulting semi-transparent Ag electrode showed a sheet resistance of $5 \Omega/\text{sq}$ and a corresponding transmission T above 30 %. It was noted that the addition of the thin ZnO nanoparticle layer lead to a significant improvement in transmission [42].

6.2.2 Metal Nanoparticles and Grids

The delivery of transmission and conductivity performance comparable to that of ITO by simply combining thin metal films with low cost printing or coating techniques in a large area device has proven to be relatively challenging. As a result, metal nanoparticle suspensions and inks have been widely explored to form metal grid based alternative electrodes that enhance conductivity without decreasing transmission [43–46]. Magdassi's group reported a simple method to achieve Ag coatings using aqueous dispersions of Ag nanoparticles in an evaporation-based lithography process applied directly onto plastic substrates [47]. As shown in Fig. 6.3, a droplet containing silver nanoparticles is placed on top of a metallic mesh; the dispersion instantaneously spreads over the mesh and plastic substrate, flows towards the wires of the mesh and dries, forming a transparent grid composed of nanoparticles. The presence of polyacrylic acid salt on the surface of the silver nanoparticles causes them to self-sinter upon short exposure to hydrogen chloride

(HCl) vapors. As a result, immediate sintering of the silver nanoparticles in the thin lines of the grid occurs even at room temperature, enabling formation of transparent, flexible conductive grid on heat-sensitive substrates. The process yields a conductive array having a very low sheet resistance, $\sim 9 \Omega/\text{sq}$, and a transparency T above 75 %. The application of this flexible conductive grid was also demonstrated in an electroluminescent device.

Jen et al., reported a spray coating method that used silver nanoparticle electrodes for inverted polymer solar cells. Here, an inverted polymer solar cell was fabricated using non-vacuum processed spray coated silver nanoparticles (Ag-NPs) as the anode electrode and compared to a vacuum deposited Ag electrode [48]. The number of spray coated layers was shown to significantly affect the final device performance; a higher number of coated layers resulted in a better nanoparticle interconnectivity and morphology. This is attributed to the fact that the reduced sheet resistance and transparency of the Ag electrode leads to improved FF, enabling a PCE as high as $\sim 3.0\%$. A comparable device fabricated on flexible ITO substrates showed a performance of only $\sim 1.4\%$.

Silver particle inks can also be used to form conducting micro grids on electrodes [49–51]. However, these inks often require complicated synthesis routes and must be annealed at high temperatures that are incompatible with most organic substrates. To overcome these limitations, several new approaches to the synthesis of silver ink precursors have recently been described. These synthetic routes are relatively straightforward and result in inks that exhibit high electrical conductivity at modest annealing temperatures [52]. One particular approach relies on the decarboxylation of a counter ion or a thermally degradable carbamate complex and yields conductivities within one order of magnitude of bulk silver [53–55]. Another approach relies on thermal activation of reducing agents above a threshold temperature [56]. Both of these inks require annealing temperatures in excess of 120°C to achieve appreciable conductivity. Lewis et al. recently described a reactive silver ink that can be activated at a much lower temperature [57–58]. This ink is prepared according to a modified Tollens' reagent synthesis using silver acetate, formic acid and ammonia. The resulting ink exhibits high conductivity at temperatures as low as 90°C . Electroninks Inc. produces the primary amine-containing modified reactive silver ink, available through Aldrich Materials Science (Aldrich Product No. 745707). In a typical procedure, silver acetate is dissolved in an aqueous solution mixture of primary amine, propylene glycol, and other humectants. Formic acid (or ammonium formate) is then added to the resultant solution in an ice-cooled water bath, followed by syringe filtering by pore size of $0.2 \mu\text{m}$ [59]. Figure 6.4a shows the particle-free ink after synthesis. Unlike the clear ink formed in the original synthesis procedure, the modified ink appears slightly yellow due to the presence of the Ag-amine complex (Fig. 6.4b). The UV-Vis spectrum shows the absorption in the region of 400–425 nm, indicating the reaction of silver and primary amine with formic acid (Fig. 6.4c). This ink is relatively stable at room temperature, and does not rapidly form silver particles until heated to $50\text{--}60^\circ\text{C}$. Figure 6.4d shows the thermogravimetric analysis (TGA) data for inks heated at 80, 100 and 120°C as a function of annealing time. Further analysis of these data reveals that the ink contains approximately 13 wt % silver.

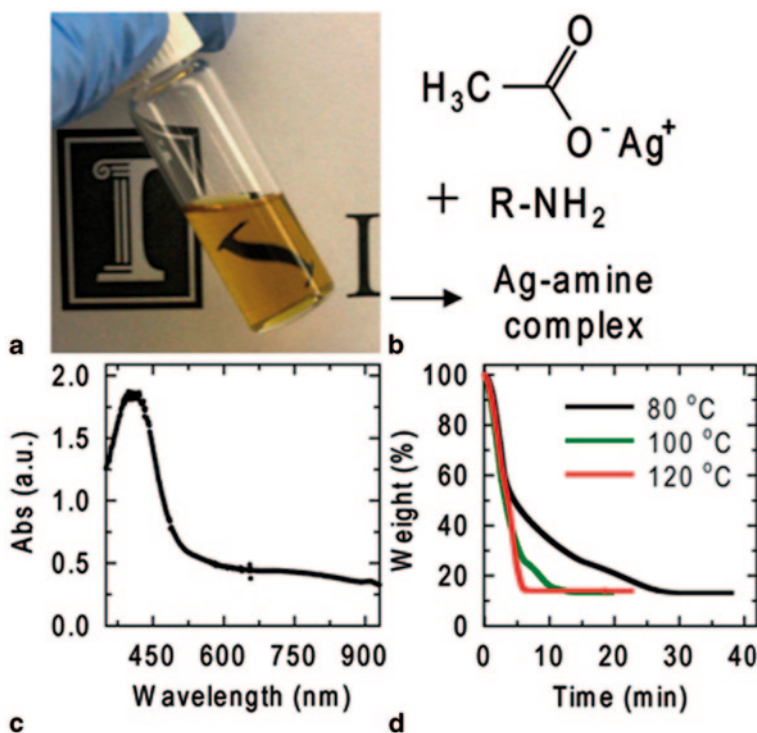


Fig. 6.4 **a** Optical image of the modified reactive Ag ink composed of 13 wt% solids. **b** Schematic illustration of the key ink constituents. **c** UV-vis absorption of the ink. **d** Thermogravimetric analysis (TGA) of the ink measured at varying temperatures as a function of annealing time. (Reprinted with permission from [59])

Figure 6.5a and b shows a single-layer grid (25×25 mm, line width = $80 \mu\text{m}$) with a line spacing of 0.5 mm printed on a poly(ethyleneterephthalate) (PET) substrate. The printed text underneath the pattern is clearly visible through the gridded substrate. Figure 6.5c shows the transmittance of grid patterns deposited with varying line spacing (0.5, 1.0 and 2.0 mm). At a grid spacing of 2 mm, a transmittance T above 90% is achieved. The patterns are produced with a single drop-width both horizontally and vertically. The ability to tailor viscosity and surface tension of this modified silver ink over a broad range facilitates multiple patterning approaches that have the potential to open new opportunities for printed electronics

One significant drawback of ink- or metal nanoparticle-based metal grid alternative electrodes is the presence of surface roughness and nano-scale peaks that can cause electric short circuits or increased sheet resistance in OPVs. To facilitate incorporation of silver inks or suspensions into OPV devices, researchers have determined that the height of any surface peaks should be less than 500 nm, while the root mean squared (RMS) roughness and spike height should be no greater than 50 nm [60]. For this reason, we will next discuss approaches that use metal grids or

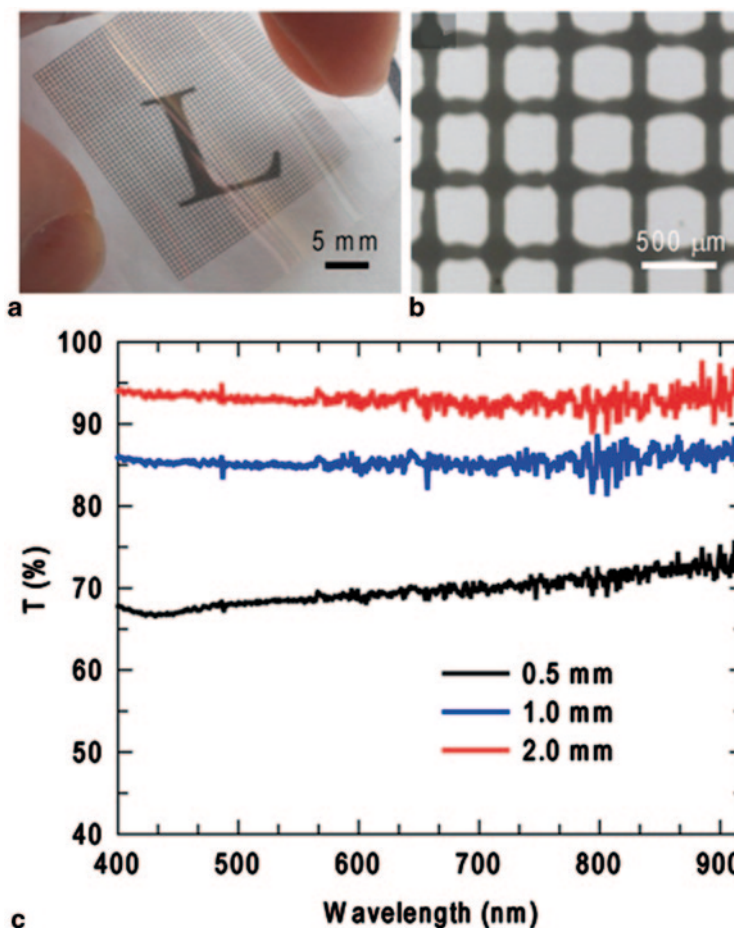


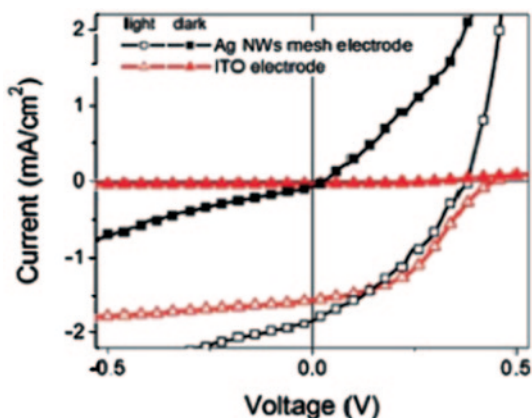
Fig. 6.5 **a** Optical and **b** SEM images of an inkjet-printed square (25×25 mm) grid with 0.5 mm spacing between $80 \mu\text{m}$ features. **c** UV-Vis transmittance of conductive grids at various grid spacing. (Reprinted with permission from Ref. [59])

nanoparticles in hybrid materials to minimize peaks and surface roughness in order to enable integration into flexible macro-electronics.

6.2.3 Silver Nanowires (Ag NWs)

Ag NWs have attracted considerable attention because they have the potential to enable an electrically conductive and flexible replacement for ITO with a high degree of transparency. Since the introduction of the polyol method [61], solution-phase methods of growing Ag NWs have progressed significantly. For example, dispersed

Fig. 6.6 Current density vs. voltage for organic photo-voltaic cells with device structure 45 nm CuPc/45 nm PTCBI/10 nm BCP/100 nm Ag on an Ag NWs mesh (squares) and ITO (triangles) in the dark (filled symbols) and under 65 mW/cm² AM1.5 illumination (open symbols). (Reprinted with permission from Ref. [64])



random networks of Ag NWs have been used to fabricate high-performance flexible transparent electrodes showing equivalent or even superior performance to ITO [62]. One of the major advantages of depositing metal nanowires onto flexible substrates is that the resulting structure can withstand far greater flexing than ITO. De et al. showed a Ag NW film with 75 % transparency and a sheet resistance of 3.4 Ω/sq (calculated FOM of this Ag NWs-based electrodes can reach as high as 350) using a nanowire density of 70 mg/m². A similar film (albeit with slightly higher nanowire density of 79 mg/m²) was shown to withstand 1000 bend cycles without any change in sheet resistance while an ITO substrate catastrophically failed after 160 bend cycles [63].

Peumans's group pioneered the solution processing of Ag NWs for use in organic solar cells [64]. Here, a random network of Ag NWs resulted in enhanced scattering of light, and improved photocurrent generation in solar cells. The inherent roughness may have also resulted in an improved donor–acceptor interface. An organic solar cell device fabricated on flexible substrates using this solution processed Ag NWs as front electrode achieved a similar performance as an equivalent ITO-based cell, as shown in Fig. 6.6.

There are still several fundamental and technical processing challenges that remain to be solved in order to fabricate an OPV device using Ag NWs. For example, the polyol method often generates low-aspect-ratio Ag nanoparticles and nanorods, which have a less substantial contribution to the electrical conductivity because they are too small to provide effective current pathways in the Ag NWs network and they cause significant optical loss due to their stronger light scattering properties [65]. Huang et al. developed a cross-flow filtration method to purify Ag NWs and remove its low-aspect-ratio by-products [66]. This continuous filtration makes it amenable to industrial scale nanowire purification, especially if large-size filters that handle thousands of liters of solution are used.

Maintaining an appropriate work function difference between the Ag NW front electrode and the Ag back electrode is necessary to obtain the large open circuit

voltage (V_{OC}) required to achieve a high PCE. You's group showed the consistently lower performance of a laminated metal nanowire electrode in regular device geometry devices compared to the ITO-based reference cells can be attributed to the lower work function difference between the Ag NWs/PEDOT:PSS and Al compared to the ITO and Al counter electrodes employed in the reference cells [67]. Tuning the work function of the electrodes with the use of buffer layers can circumvent these problems. Peumans and McGehee et al. demonstrated the use of Cs_2CO_3 to alter the work function of metal back electrodes in a P3HT:PCBM-based inverted structure and obtain a PCE of 2.5% [68]. Leem et al. used optically transparent TiO_2 as a buffer layer on top of Ag NWs layer in an inverted solar cell and achieved a similar performance as that of an ITO-based reference cell with a PCE of 3.45% [69]. It was also shown that such a buffer layer effectively reduces the surface roughness of the electrode and suppresses the formation of shunt paths. Without a buffer layer, devices normally have a high V_{OC} , but the FF and the short circuit (j_{SC}) are substantially lower. ZnO can also be used as a buffer layer in an inverted solar cell with Ag NWs as the front electrode. The PCE obtained for these Ag NW-based devices was shown to be higher or similar to that of their comparable ITO-based cells [70, 71]. Stubhan et al. employed Ag NWs/ZnO buffer layer electrodes with a photoactive layer of poly(3-hexylthiophene) (P3HT) and [6,6]-phenyl-C61 butyric acid methyl (PCBM) and achieved FF of over 62% and a PCE of $\sim 2.7\%$ [72].

The poor adhesion of nanowires to substrates is one of the major issues of processing and must be addressed to enable large-scale fabrication and wide application. In fact, an overcoating or additional treatment is typically required to achieve adhesion between the Ag NWs film and the substrate. Methods such as heating [73], pressure treatment [74], and surface modification [75] have been used to obtain an adherent, optically transparent and electrically conductive film comparable to commercial ITO. For example, Jiu et al. demonstrated a rapid sintering technique by applying high-intensity pulsed light to sinter the Ag NWs film and thus achieve strong adhesion and even high conductivity on flexible polymer substrates including PET, PC and PVC [76]. Figure 6.7 shows typical UV-vis spectra of Ag NWs films on glass and PET substrates. A transmittance of 82.8% at 550 nm was achieved. The conductivity of the Ag NWs film can be further enhanced through light sintering, reducing a sheet resistance from over 1000 Ω/sq down to $\sim 20 \Omega/sq$.

Voids between individual Ag NW in the film limit the conductivity and charge extraction properties of electrode, particularly when the voids are larger than the charge carrier diffusion length. Filling these voids with highly conductive ZnO leads to semi-continuous film formation and suppresses charge recombination, ultimately improving PCE. Ajuria et al. reported a PCE of $\sim 3.9\%$ on glass and $\sim 3.2\%$ on PET using Ag NWs/ZnO front electrodes compared to ITO-based cells with ZnO buffer layer that showed a PCE of $\sim 3.5\%$ [58]. On the other hand, Ag NWs films often suffer from 'haziness' caused by surface roughness, which must be minimized to realize practical implementation of Ag NWs networks as transparent conductors. Coskun et al. reduced the surface roughness of Ag NWs networks from 54 to 5 nm through optimization of the low temperature annealing treatment and planarization by PEDOT: PSS. This produced Ag NWs films with transmittances and sheet

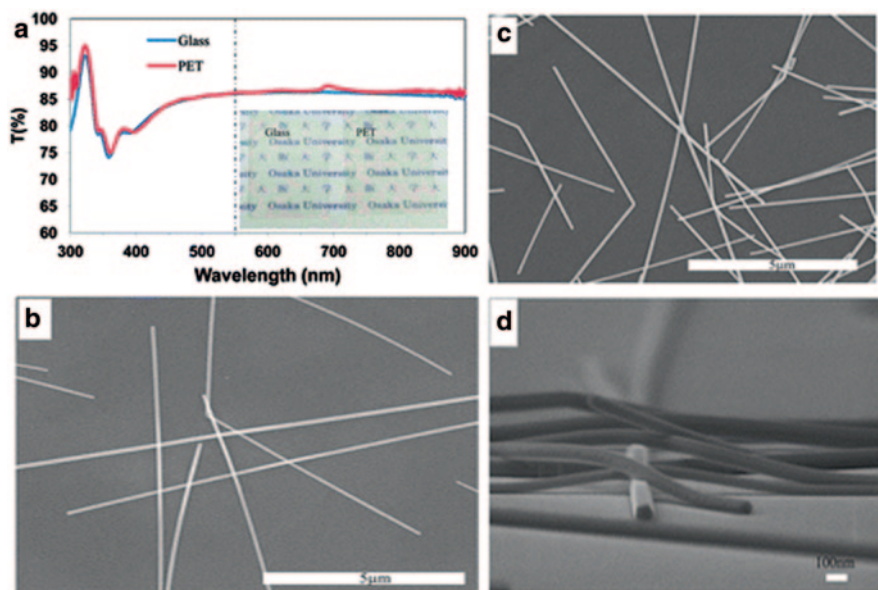


Fig. 6.7 **a** Transmittance spectra of Ag NWs films on glass and PET substrates. The inset shows a photo of the Ag NW film on both substrates, **b** SEM image of Ag NWs on glass **c** SEM image of Ag NWs on PET **d** SEM images showing the tilted cross-sectional of Ag NWs on PET substrates. (Reprinted with permission from Ref. [76])

resistances of 87% and 11 Ω/sq , representing some of the best values for FOM ($=240$) reported for non-oxide-based transparent conductors [77].

Research on Ag NW films is currently in a stage of rapid development. At this point, the development of a suitable solution-based processing method still remains a significant barrier to solve before Ag NWs become a low cost, mass market technology and replace ITO. To address this, a large part of research on Ag NWs is currently directed towards developing large scale compatible processing techniques [74, 78–80]. Lim et al. used direct brush-painting of Ag NWs onto a PET substrate to achieve network electrodes with a low sheet resistance of $\sim 39 \Omega/\text{sq}$, a high diffusive transmittance of $\sim 88\%$, superior mechanical flexibility and identical performance to those OPV devices with conventional ITO electrodes [62]. Hauger et al. described a route of spray-coating Ag NWs meshes on PET sheets that are treated with a straightforward combination of heat and pressure to generate electrodes with low sheet resistance, good optical transmission, flat topology and strong adherence to the PET substrate [81]. The as-sprayed Ag NW mesh electrodes are highly resistive due to poor contact between the individual Ag nanowires. However, upon application of light pressure using a stainless steel rod, Ag NWs mesh arrays on PET achieved sheet resistances of $< 20 \Omega/\text{sq}$. Bending of these rolled nanowire meshes on PET with different radii of curvature (ranging from 50 to 0.625 mm) showed no degradation. Repeated bending (100 times) around a rod with a radius of curvature of 1 mm also resulted in no increase in sheet resistance, demonstrating good

adherence and no signs of delamination of the NW mesh array. Similarly, Scardaci et al. demonstrated spray coated Ag NWs networks with typical transmittance T of $\sim 90\%$ and sheet resistance of $\sim 50 \Omega/\text{sq}$ [82]. Incorporating such spray coated Ag NWs mesh electrodes into OPV devices resulted in only slightly lower efficiency than the referenced ITO benchmark, while rolled Ag NWs electrodes also showed a very good device yield, an important factor for reducing the cost of large area manufacturing.

Apart from academic efforts, several industrial breakthroughs have been made to produce Ag NWs-based TCEs for use in next-generation consumer devices. Cambrois, a Silicon Valley based company, commercialized a directly patternable and wet-processable transparent conductive film, ClearOhm™, made from Ag NWs. Heliateck, a Germany-based organic solar cell technology company, applied ClearOhm™ conductive films in a vacuum deposited pin-tandem cell ($> 1 \text{ cm}^2$) on PET substrates, and achieved high FF, low series resistance, low leakage current and overall $\sim 8.5\%$ PCE [83]. Similarly, Carestream Advanced Materials developed transparent conductive films (FLEXX®) based on Ag NW technology, solution-coating chemistry, and using continuous R2R processing on $125 \mu\text{m}$ optical grade and 500 mm wide PET sheets. The company claims its films can achieve sheet resistance of $\sim 100 \Omega/\text{sq}$ and transmission of over 89% [84].

Though Ag NW technology is a promising candidate for ITO replacement, the abundance of silver is comparable to that of indium. Problems with the supply of indium may foreshadow future supply problem for silver. Alternatively, the use of nanowires made from alternative metals, such as copper, has been demonstrated. For example, electrospun copper NWs were used to fabricate high-performance electrodes with a high aspect ratio of $100,000$ and 90% transmittance at $50 \Omega/\text{sq}$ [85]. Developments like these may open additional routes for transparent electrodes.

6.3 Organic and Carbon-Based Alternative TCEs

6.3.1 PEDOT:PSS

OPVs represent the latest generation of solar power generation technologies, with the advantages of lightweight, transparent and flexible polymeric conductive electrodes that enable low-cost and highly automated R2R mass production processes [12]. Among conductive polymers, poly(3,4-ethylenedioxythiophene):poly(4-styrenesulfonate) (PEDOT:PSS) has emerged as the leading material for use in TCEs. Among its many advantages, PEDOT:PSS can be tailored to the desired manufacturing and printing technologies such as slot die coating, spin coating, inkjet or screen printing [86, 87].

PEDOT:PSS is a water dispersible form of the intrinsically conductive PEDOT polymer. Figure 6.8 shows the polymerization of EDOT monomer in the presence of polystyrene sulfonic acid (PSS), which is added as a charge balancing counter

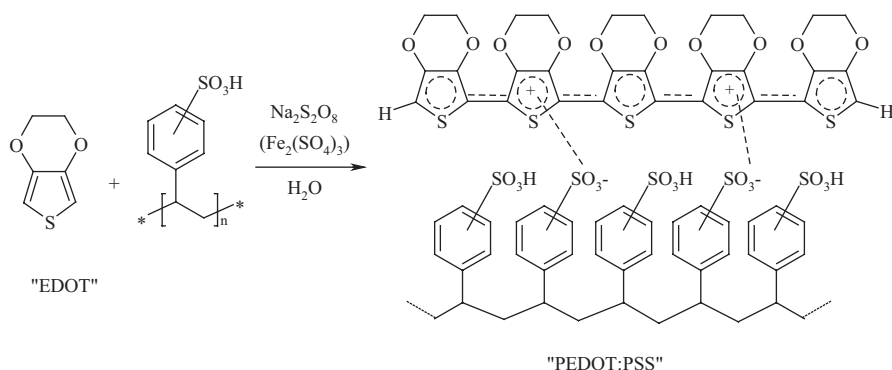


Fig. 6.8 Synthetic route and chemical structure of PEDOT:PSS

ion to improve the inherently low solubility of PEDOT, resulting in an aqueous PEDOT:PSS dispersion. Compared to other conducting polymers, PEDOT:PSS has a fairly high conductivity and transparency. This is because the p-conjugation of PEDOT provides semiconducting properties while the PSS acts as a p-type dopant, raising the room temperature conductivity from a typical value of 100–1000 S/cm with proper optimization. In addition, the ability to apply PEDOT:PSS to flexible substrates enables cost-effective R2R mass production [88, 89], making it a very promising material for optoelectronic organic devices.

OPV cells are typically comprised of a number of layers, including the anode layer, hole injection layer (HIL), photoactive layer, electron transport layer (ETL) and cathode layer. OPVs are commonly configured in one of the two different OPV geometries: regular and inverted geometry as shown in Fig. 6.9. The anode in a regular cell typically is ITO and the cathode is a metal that has a lower work function than ITO (e.g. aluminium, lithium). In the case of an inverted cell, ITO forms the cathode and the anode is a metal with a work function higher than ITO (e.g. silver). Both geometries have advantages and drawbacks. Regular OPV cells are easier to scale and require fewer layers. Inverted OPV cells are more stable and generally show higher efficiencies.

PEDOT:PSS was first used in the regular geometry device structure as a HIL layer to facilitate the selective transport of holes to the anode layer and to reduce the potential for electrical shorts that can be caused by the surface roughness of the anode layer. Similar to other materials that follow the Beer–Lambert Law, PEDOT:PSS exhibits a trade-off between transmission and conductivity. The lack of conductivity of PEDOT:PSS at high light transmission is a major obstacle; typical conductivity values for PEDOT:PSS are around 1–10 S/cm, which is three orders of magnitude lower than that of ITO (>4000 S/cm) at similar transmission (80%) [90]. Furthermore, PEDOT:PSS films with a comparable sheet resistance to ITO (10–20 Ω/sq) only transmit 10–30% of light [91]. The trade-off between transmission and conductivity ultimately results in poor PCEs for ITO-free OPVs

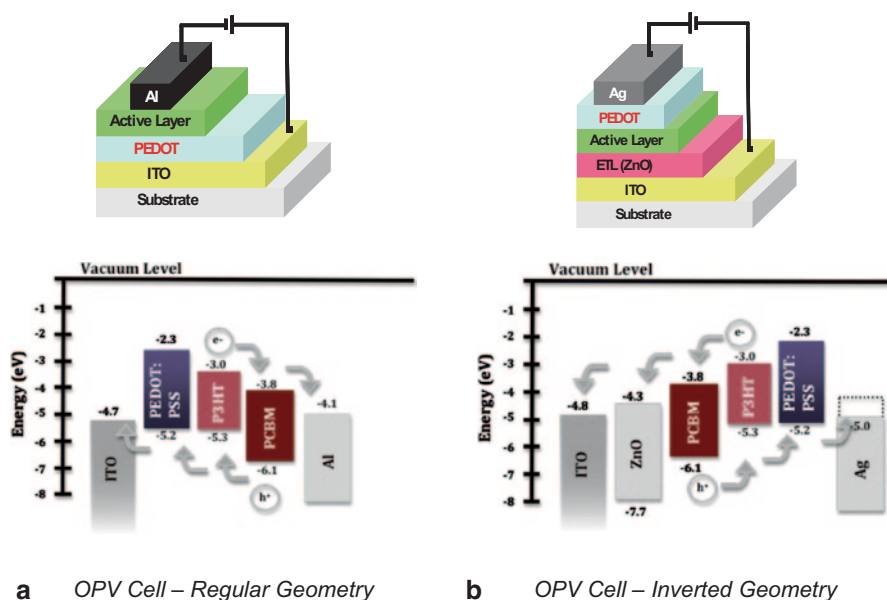


Fig. 6.9 OPV architectures and corresponding energy level diagrams for **a** regular geometry and **b** inverted geometry. (Adapted from Ref. [98])

that use PEDOT:PSS. A number of strategies have been explored to further increase the conductivity of PEDOT:PSS, including manipulation of synthetic conditions, modification of the functionality of the polymer backbone and the addition of high boiling point polar components such as dimethylsulfoxide (DMSO), glycerol, ethylene glycol or sorbitol to the formulation [92–95]. These high conductivity grade PEDOT:PSS formulations have helped to increase the efficiencies of ITO-free regular geometry OPV cells fabricated on glass and on flexible plastic substrates, achieving 3.27 and 2.8%, respectively. Comparable ITO-based devices achieved 3.66 and 2.9% [96].

When used in the inverted geometry, PEDOT:PSS becomes the hole collecting back electrode while ITO serves as the front electrode. As shown in Fig. 6.9b, the inverted configuration does not require transmission through the PEDOT:PSS layer, so the thickness can be increased to maximize conductivity. Typically, the thicker the PEDOT:PSS film is, the higher conductivity until saturation is reached [89, 97]. A predicted layer thickness contour plot based on viscosity and rotation speed is given in Fig. 6.10 for spin coating applications. In a currently preferred inverted geometry, the metal grid is printed on top of the PEDOT:PSS. This enables the manufacturing of transparent OPV devices by applying both bottom and top transparent (grid) electrodes combined with a thin PEDOT:PSS layer, completely replacing the ITO electrode. The use of a combination of multiple organic-inorganic materials for alternative transparent electrode is discussed in the next section.

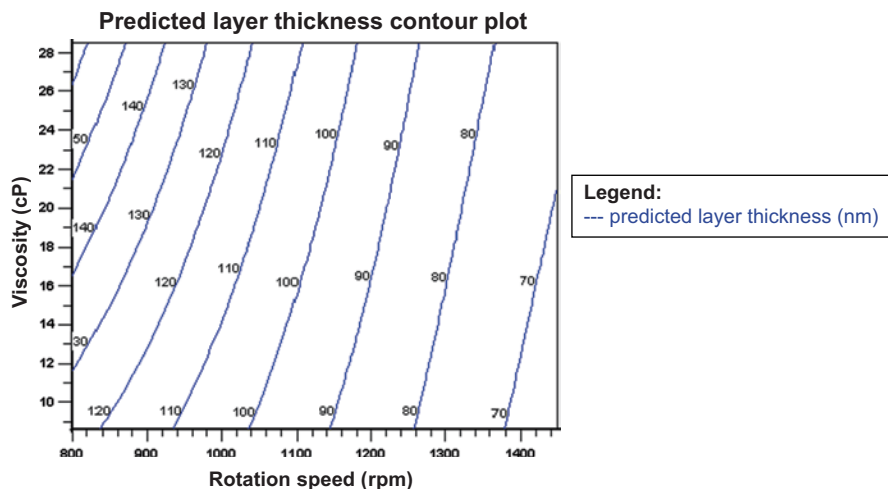
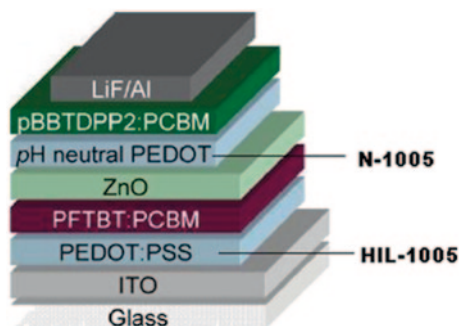


Fig. 6.10 Predicted layer thickness contour plot. (Reprinted with permission from Ref. [99])

Fig. 6.11 Tandem solar cell.
(Adapted from Ref. [100])



To even further improve the efficiency of OPV systems, new architectures such as multilayer tandem solar cells have been developed to absorb more of the solar light spectrum (Fig. 6.11). In a conventional single-junction OPV cell, photons with energies smaller than the bandgap cannot be absorbed and photons with larger energies lose their excess energy via thermal equilibration. Tandem solar cells can reduce these losses by combining separate sub-cells each absorbing a different part of the solar spectrum. In a tandem solar architecture, a stack of ZnO vapour deposited or solution-processed nanoparticles and pH-neutral PEDOT:PSS (Orgacon N-1005 (Aldrich Prod. No. 739324)) are used as a recombination layer. With the aid of wide- and small-bandgap polymers as the photoactive layer, the optimized tandem solar cells have achieved an efficiency of 4.9% [100]. OPV tandem cell with higher transparency and efficiency are expected to be useful for applications such as building integrated photovoltaics (BIPV).

The availability of highly conductive formulations of PEDOT:PSS enabling more rigorous device testing and stimulating commercial development. For example, the latest generation of Heraeus Clevious™ PH500 and PH1000 have a conductivity of 300 and 850 S/cm, respectively. Aldrich Materials Science worked with Agfa to introduce the Orgacon™ OPV product portfolio to the research market. Slot die and spin coating formulations as well as inkjet and screen printing inks are available. Orgacon HIL-1005 (Aldrich Prod. No.768642) and IJ-1005 (Aldrich Prod. No.739316) have been specifically designed to be used as HIL materials and can be applied using slot die coating, spin coating or ink jet printing. The formulations are optimized for coating on surfaces such as glass, PET, PEN or photoactive materials (e.g. P3HT/PCBM). Surface tension can be optimized if needed by adding very small amounts of non-ionic surfactants. Alcohols such as isopropyl alcohol (IPA) can also help to optimize the wetting properties, for example onto P3HT/PCBM. Orgacon N-1005 (Aldrich Prod. No.739324) is a pH-neutral PEDOT:PSS formulation for use in tandem OPV cells as a recombination layer and can be applied with slot die and spin coating. Orgacon S305 (Aldrich Prod. No.739340) and Orgacon EL-P 5015 (Aldrich Prod. No.768650) screen printing inks are especially effective for applications where an ITO alternative is needed, and can be applied by printing on a metal grid to form a highly transparent anode. Detailed properties and performance comparison is shown in the Table 6.1 below.

6.3.2 CNTs

Carbon nanomaterials, such as single-wall carbon nanotube (SWCNTs), multi-walled carbon nanotubes (MWCNTs) and graphene, are versatile materials that can play many different roles in photovoltaics and offer promise for significantly increasing the functionality and performance of next-generation solar cells.

Since their discovery in 1991 by Ijima [101], SWCNTs have stimulated a great deal of activity in both the global research community and industry, and have inspired significant investment to develop the required manufacturing, characterization and application capabilities. Individual SWCNT can have a current conductivity of 10^6 S/m and mobility of 10^5 cm²/V s [102], current carrying capacities of 10^9 amp cm⁻², which are higher than those of copper or gold [103]. They also have a characteristic optical absorption and fluorescence response such that each chirality demonstrates its own characteristic absorption and fl film as a transparent p-contact uorescence spectrum. In terms of mechanical properties, SWCNTs are significantly stronger than steel. Theoretical tensile strength values of SWCNTs are ~100 times greater than steel at 1/16th the weight, although the highest value actually measured is approximately half of the predicted theoretical strength due to structure defects [104]. Rinzler's group first reported the use of a 100 nm thin SWCNT film as a transparent p-contact in a GaN LED, achieving a 60% transmission. Later the group fabricated a 50 nm thin film of p-doped SWCNT film, achieved a sheet resistance of 30 Ω/sq and a transmission of >70% in the visible region of the light spectrum. This and other similar films are shown in Fig. 6.12 [105].

Table 6.1 Orgacon™ materials for flexible OPV

Product	Solid Content (%)	pH	Viscosity (mPa × s)	Surface tension (mN/m)	Surface resistance (Ω/sq) ^a	Work function (eV)	Process	Application
Orgacon™ HIL –1005 (Aldrich Prod. 768642)	1.0	1.9	10	34	110	5.2–5.4	Slot die and spin coating	HIL
Orgacon™ IJ –1005 (Aldrich Prod. 739316)	0.8	2.0	10	33	110	5.2–5.4	Inkjet printing	HIL
Orgacon™ S305 (Aldrich Prod. 739340)	0.8	2.3	17	19	130	N/A	Slot die coating screen printing	ITO alternative
Orgacon™ EL-P 5015 (Aldrich Prod. 768650)	5.0	1.5	113 000	N/A	635	N/A	Screen printing	ITO alternative
Orgacon™ N –1005 (Aldrich Prod. 739324)	1.2	7.0	36	52	170 ^b	N/A	Slot die and spin coating	Tandem cell

^a Coated layer with 90 % transmission at 550 nm, without substrate absorption and reflection losses

^b High boiling solvent added

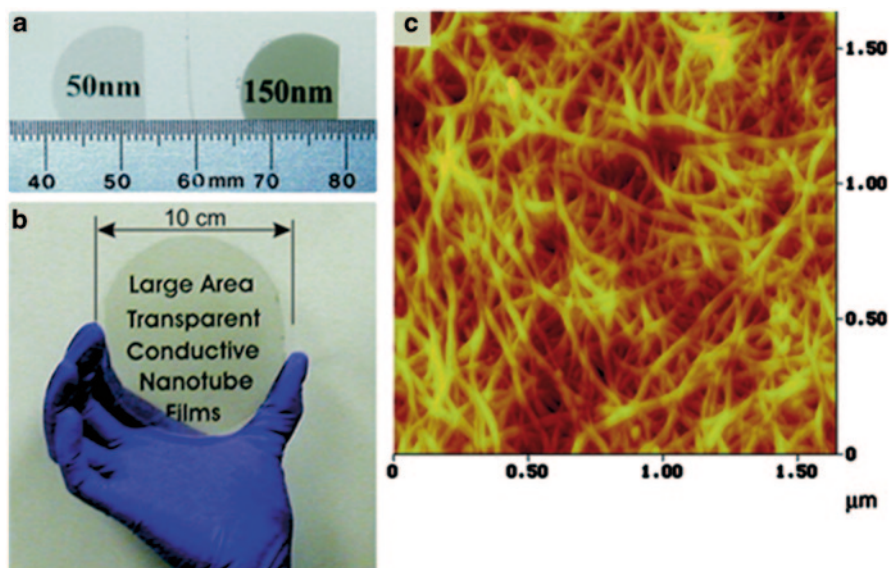


Fig. 6.12 Transparent SWCNT films. **a** Films of the indicated thickness on quartz substrates. **b** 80-nm-thick, large area transparent conductive film formed from nanotubes on a 10 cm diameter sapphire substrate. **c** AFM image of a 150-nm-thick t-SWNT film surface (colour scale: black to bright yellow, 30 nm). (Adapted with permission from Ref. [105], copyright 2004 Science)

There still remain a number of technical hurdles that have so far limited the widespread applications of SWCNTs on TCEs. These hurdles include purity, selectivity and dispersibility. For example, the various manufacturing processes used in the production of SWCNTs lead to products that are contaminated to varying degrees with residual catalyst and other forms of carbon. Also as described above, as produced SWCNTs are a mixture of tubes with different chiralities, two third of which are metallic (electrically conducting) and one third are semiconducting. The presence of metallic SWCNTs causes electronic shorts in semiconductor device applications and dramatically degrades device performance. In TCE applications, undoped semiconducting SWCNTs cause troublesome non-ohmic contacts in films. This conductivity can be reduced by adsorption of molecular charge transfer dopants, such as p-doping by acidic molecules (e.g. HNO_3 , SOCl_2) [106] and n-doping by basic molecules (e.g. hydrazine, ethylenediamine) [107]. Thus, in order to fully realize their potential performance, SWCNTs must be both highly pure and have homogeneous electronic properties. To meet these demands, as produced SWCNTs must be purified to remove impurities and then separated to produce monodisperse samples. A breakthrough separation method was pioneered by Arnold and Hersam in 2006 [108]. The density gradient ultracentrifugation (DGU) method successfully enabled the sorting of SWCNTs-based on the number of walls, diameter, electronic type, chirality and chiral handedness (left- vs. right-handed SWCNTs). To accomplish this, SWCNTs are first solubilized in water using surfactants that bind preferentially to specific types of SWCNTs. Next, SWCNTs are separated

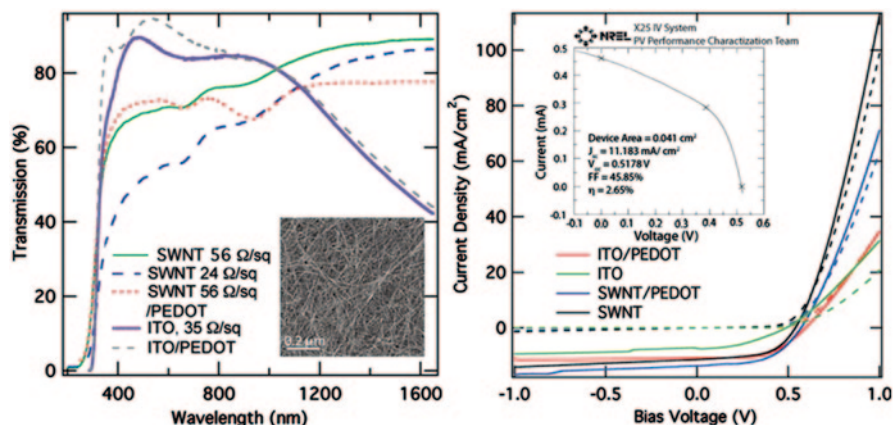


Fig. 6.13 *Left*: Transmission spectra for transparent electrodes (with and without PEDOT) used for device fabrication. Inset: inverted-contrast transmission electron microscopy image of sprayed SWNTs. *Right*: Light (solid lines) and dark (dashed lines) J - V curves for devices on SWNT and ITO transparent electrodes, with and without PEDOT as an HTL. Inset: NREL-certified light I - V data for BHJ device on a SWCNT electrode without an HTL (PEDOT:PSS). (Reproduced with permission from Ref. [111], copyright American Institute of Physics)

by centrifugation of the solution in a density gradient until the nanotubes reach their equal-density positions within the gradient and can be physically isolated. The DGU process has been scaled up commercially by NanoIntegris. Aldrich Materials Science distributes both 98 % metallic SWCNTs (Aldrich Product No. 750530) and 98 % semiconducting SWCNTs (Aldrich Product No. 750522) produced by this methods for use by researchers worldwide.

Although the carrier mobility in a single, isolated SWCNT is extremely high, tube-tube junctions between neighbouring SWCNTs limit the carrier mobility in TCEs. Temperature-dependent resistance measurements have shown that the magnitude of inter-tube barrier resistance decreases according to the following sequence: undoped semiconducting SWCNTs, undoped and doped metallic SWCNTs, semiconducting SWCNTs [109]. Reducing the magnitude of the transport barrier experienced by carriers at these junctions is critical to further increasing the conductivity of SWCNT-based TCEs. Much recent progress has been made to address this key issue. Tenent and Barnes et al. reported a sheet resistance of 110 Ω/sq with transmission of 78 % (550 nm) on undoped SWCNTs films and 37 Ω/sq with transmission 76% on doped SWCNTs films, as shown in Fig. 6.13 left [110, 111]. Without using PEDOT:PSS as an HTL layer, the corresponding OPV device (Glass/SWCNT/P3HT:PCBM/Ca/Al) achieved an NREL-certified efficiency of 2.65 % and a short-circuit current density of 11.2 mA/cm², as shown in Fig. 6.13 right.

To overcome the high roughness of SWCNT films and achieve high performance OPV devices, the photoactive material layer must be made to be 500–800 nm thick, thicker than required for efficient absorption of sunlight [112]. McGehee et al. developed a PDMS-based transfer-printing method to make homogeneous, relatively

smooth SWCNTs TCE films on flexible PET substrates without the use of thick active layers [113]. This method results in significant improvement of the RMS surface roughness evaluated by an atomic force microscopy (AFM) probe (less than 10 nm over a surface of $25 \mu\text{m}^2$). The SWCNT films show transmission of 85 % in visible light region and a R_s of $200 \Omega/\text{sq}$. The improved TCE film properties enable the fabrication of conjugated polymer based bulk heterojunction solar cells that nearly match the performance (PCE: 2.5 %) of ITO-based reference devices (PCE: 3 %).

Another challenge for widespread application of SWCNT-based TCEs is the processing of large area films. To date, spray deposition has proven to be the most scalable and cost effective method. SWCNTs can be dispersed in aqueous solvents with the aid of surfactants, such as high molecular weight sodium carboxy methyl cellulose (CMC, 90000 MW) [110, 114]. The dispersion can be deposited over large areas (6×6 in.) by ultrasonic spraying followed by exposure to nitric acid to ensure removal of the CMC while simultaneously p-doping the nanotubes. Such a film has a very low RMS roughness (3 nm scanned over $100 \mu\text{m}^2$ area) with superior electrical conductivity and optical transmission, resulting PCE of 3.1 % comparable to ITO-based reference devices (PCE of 3.6 %).

Further, the weak adhesion of SWCNTs onto the glass substrates can be improved by dip-coating the bare glass substrate in a 1 % solution of 3-aminopropyltriethoxy silane in deionized water to form cross-linked siloxane to the surface. The optimized device has a sheet resistance $51 \Omega/\text{sq}$ with a transmission of 69 % (at 550 nm) and has a PCE of 3.6 and 2.6 %, respectively, on glass and PET substrates. This is the highest reported performance of OPVs using SWCNTs as TCEs [115].

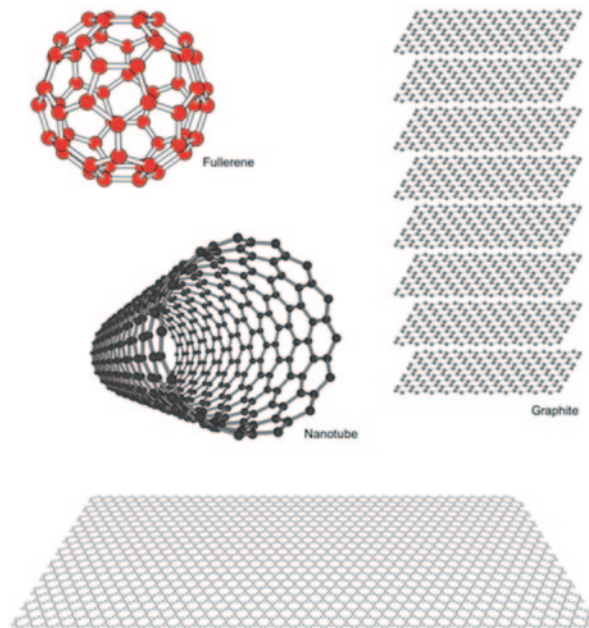
The simplified processing techniques enabled by MWCNTs also make possible their use as opaque organic solar cell anodes [116] and transparent electrodes [117]. However, the use of MWCNTs results in even rougher topology compared to SWCNT films. As a result, MWCNTs usually require a thicker planarization layer is required and this results in less light transmission to the photoactive layer. Therefore, the use of MWCNTs typically yields a lower PCE than SWCNT in a regular device structure.

On the commercial side, Aldrich Materials Science has partnered with Southwest Nanotechnologies to formulate aqueous conductive CNT inks (Aldrich Product Nos. 791490 and 791504) optimized for screen printing techniques such as spray and slot die coating, using patented CoMoCAT® technology. These inks dry quickly even at low temperature and adhere strongly to common screen printing substrates. The films made from such inks have sheet resistance of $130\text{--}330 \Omega/\text{sq}$ and transmission T above 85 % over visible region of the light spectrum, setting a new standard for the performance of transparent conductors in applications where durability and environmental stability are critical.

6.3.3 Graphene

Graphene is a single layer of sp^2 carbon atoms bonded in a honeycomb lattice structure, and can viewed as the building block for many different carbon nanomateri-

Fig. 6.14 Graphene is the building block of other carbon materials. (Reprinted with permission from Ref. [99])



als with various dimensionalities as shown in Fig. 6.14. If wrapped up into a ball, zero-D fullerene is obtained; when rolled, one-D nanotube; and if stacked, three-D graphite is obtained.

Graphene has remarkable properties: its intrinsically high electron and hole mobility values ($> 10^5 \text{ cm}^2 \text{ V}^{-1} \text{ s}^{-1}$), even at room temperature, enable high electrical conductivity [118]; high thermal conductivity ($> 4000 \text{ W m}^{-1} \text{ K}^{-1}$) [119], chemical stability and high mechanical strength (300 times higher than steel). These characteristics make graphene capable of meeting the need of flexible electronics [120]; and capable of use in harsh environments. With less than 0.1% reflectance and 2.3% absorbance for every single layer, graphene is transparent from the entire visible through far IR region; the theoretical transmission limit of a monolayer graphene sheet is 97.7% [121, 122]. The minimum sheet resistance of a theoretical undoped mono-layer graphene is about $30 \text{ } \Omega/\text{sq}$ (free-standing mono-layer graphene with room temperature mobility of $2 \times 10^5 \text{ cm}^2 \text{ V}^{-1} \text{ s}^{-1}$ and carrier concentration of 10^{12} cm^{-2}), making graphene a promising material for TCE applications. Undoped monolayer graphene TCE (e.g. Aldrich Prod No. 773719) shows $600 \text{ } \Omega/\text{sq}$ with a $T < 97\%$. De et al. predicted an upper limit for R_s of undoped graphite films, e.g. multi-layer graphene, at $337 \text{ } \Omega/\text{sq}$ with a $T = 90\%$ [33]. For highly doped graphene,

$$R_s = \frac{62.4}{N} \text{ } \Omega/\text{sq} \quad (6.8)$$

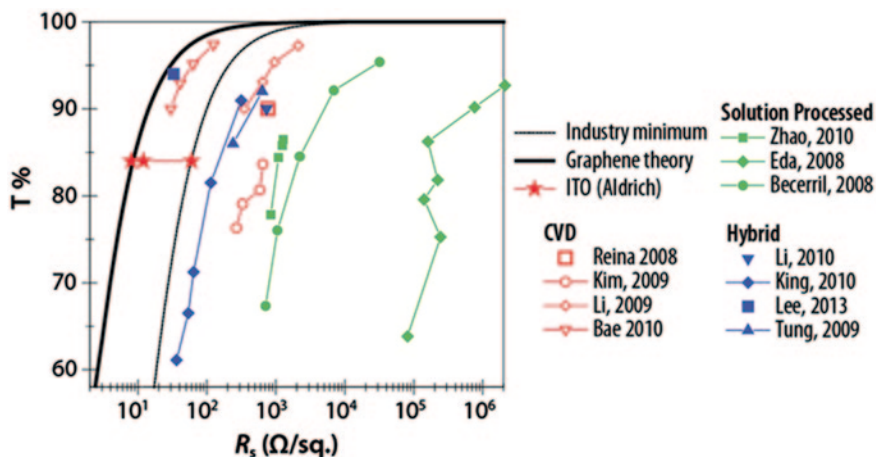


Fig. 6.15 Transmittance and sheet resistance data reported in the literature. Data shown are for graphene films prepared by CVD (open red), solution processed graphene (solid green), and hybrid graphene film (solid blue). The red stars represent commercially available ITO. The dashed line illustrates the minimum industry standard for TCE (FOM=35). The solid line corresponds to the calculated case of highly doped graphene (FOM=244). (Reprinted with permission from Ref. [124])

where N is the number of graphene layers in the film [123]. The theoretical transmittance of a free-standing graphene can be derived by applying the Fresnel equations, giving $T = 100 - 2.3 N$ (%) depending on the number of layers N . The absorbance per layer of graphene is then calculated to be $A = 1 - T = 2.3\%$ [38]. Therefore, four-layer graphene result in an R_s of $15 \Omega/\text{sq}$ with a $T \sim 90\%$, sufficient for most transparent conductor applications.

Yu and Chen compared FOM values calculated from the literature for graphene-based TCEs prepared using a variety of methods [124]. The sheet resistance and optical transmittance data from the literature were extracted and fitted using Eq. 6.5, together with the calculated FOM, and plotted in Fig. 6.15.

At this time, high quality graphene is produced by either micromechanical cleaving or grown by chemical vapour deposition (CVD). Neither of these methods is considered sufficiently scalable or cost-effective for commercial use. Bottom-up growth of CVD graphene on metal (mainly Ni and Cu) catalytic substrates can result in quality large-area thin films that closely match that of micromechanically exfoliated graphene from highly oriented pyrolytic graphite. Kong's group and Hong's group reported the growth of graphene on a polycrystalline Ni film [125, 126]. The as-grown graphene film can be transferred to glass or plastic substrates by a poly[methyl methacrylate] (PMMA) [125] or polydimethylsiloxane (PDMS) [126] layer or simply left on the PDMS surface as a flexible or stretchable film (Fig. 6.16a). The resulting TCEs have $R_s \sim 900 \Omega/\text{sq}$ with a $T = 90\%$ and $280 \Omega/\text{sq}$ with a $T = 76\%$, respectively. Similarly, graphene TCEs derived from CVD on Cu foil show better performance than that from the Ni foil and can exhibit $R_s \sim 350 \Omega/\text{sq}$ with a $T = 90\%$ [127]. The reason for the better properties of the Cu foil-derived

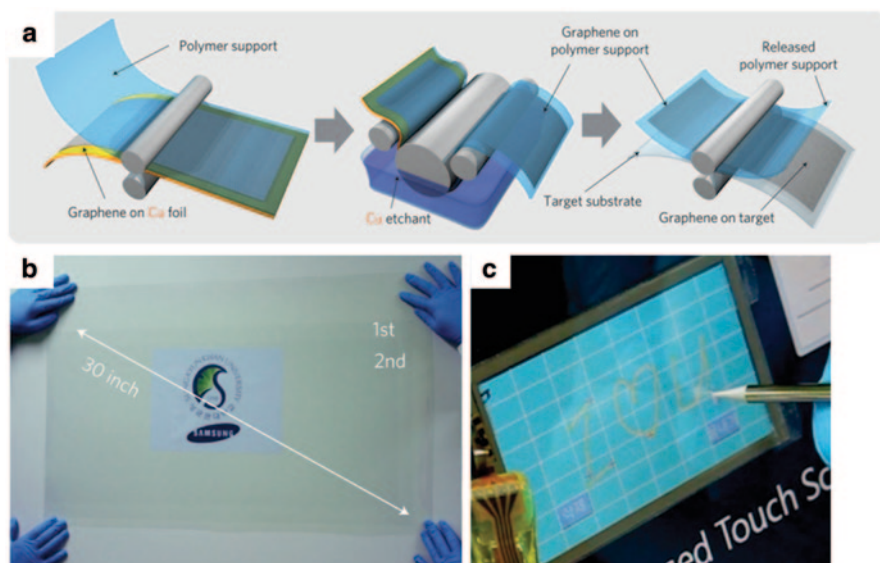


Fig. 6.16 **a** Schematic of the R2R transfer of graphene films grown on a Cu foil. **b** A transparent ultra large-area graphene film transferred on a 35 in. PET sheet. **c** A graphene-based touch-screen panel connected to a computer with control software. (Reprinted with permission from Ref. [131], copyright 2010 Nature)

films is that the as-grown graphene on Cu is almost homogeneously single layer, while the graphene film on Ni has a varying number of multiple layers [128].

The use of low pressure CVD is already well-established within the modern microelectronics industry, and a number of initiatives are underway to develop R2R-based CVD manufacturing for the low-cost, mass production of graphene films [129, 130]. Bae et al. recently made a breakthrough towards enabling the real industrial application of TCEs using large-area graphene by growing graphene on a Cu foil and then transferring it to a PET film using a R2R technique [131]. As shown in Fig. 6.16, the R2R transfer of a graphene film grown on a flexible 30 in. PET substrate can be used to achieve excellent optoelectronic performance across the entire substrate. With a four-layer p-doped graphene produced through repeated transfers, the TCE exhibits $R_s \sim 30 \Omega/\text{sq}$ with a $T=90\%$. These graphene-based TCEs already outperform ITO in some aspects and therefore make CVD graphene a very promising material for practical applications.

Solution-based processing is another technique that currently pursued for the large scale and low-cost production of graphene-based TCEs. Similar to the process used for fabricating SWCNT TCEs, the solution process is a top-down method involving two steps: first breaking the graphite down to graphene flakes and then applying the graphene thin film onto the substrate. The first step, chemical exfoliation of graphene oxide (GO), is a mature technique that can be carried out by oxidizing inexpensive graphite powders using strong oxidants, followed by gentle exfoliation to obtain separated flakes. After purification by washing,

filtering, centrifuging and re-dispersing in water, a stable and clear aqueous GO suspension can be obtained. The second step in the process, fabrication of the graphene thin-film, can be completed by either spin coating [132], rod coating [133], filtration-transfer [134], the Langmuir–Blodgett (LB) film technique [135], or by self-assembly [136]. As-fabricated GO film contains a high coverage of oxygen-containing groups, making it insulating. As a result, the GO thin film must be further converted to reduced graphene oxide (rGO) to enable electrical conduction [137]. Increasing rGO sheets to $7000 \mu\text{m}^2$, Zhao et al. have reported a TCE with $840 \Omega/\text{sq}$ at 78 % transmittance [136].

The rigorous oxidation or ultrasonic cleaving required for solution processing results in unavoidable breakage leading to very small graphene sheets (mostly with an area on the order of $100 \mu\text{m}^2$). As a result, large sheet resistances arise due to numerous small-size grains, grain boundaries and defects. Thus, the solution-processed graphene sheets typically exhibit poor electronic properties with sheet resistance in the thousands of ohm square range [138] and poor interlayer contact due to inter-flake junctions analogous to those found in SWCNTs networks [139]. Although much effort has been devoted to development of an improved reduction technique, none can fully reduce GO and restore the exact graphene structure. Without the removal of the structural defects found in the solution-processed graphene sheets, further efforts to improve the performance of solution-processed TCEs are not expected to lead to further breakthroughs.

A number of researchers have managed to produce pristine, defect-free graphene flakes by altogether avoiding oxidization and reduction in the liquid-phase. For example, Coleman et al. pioneered the liquid-phase exfoliation of pristine graphene from bulk graphite in the organic solvents *N*-methylpyrrolidone (NMP), *N,N*-Dimethylacetamide (DMA), γ -butyrolactone, and 1,3-dimethyl-2-imidazolidinone (DMEU), which are known for exfoliation of CNTs [140]. The ultrasonically-cleaved graphene flakes form a stable suspension in the liquid phase with the assistance of a surfactant. Green et al. prepared graphene by ultrasonication of graphite in water with the assistance of a planar surfactant sodium cholate [141]. Blake et al. simply exfoliated graphite by sonication in dimethylformamide (DMF) and obtained a well-dispersed suspension [142]. While promising, these techniques still cannot bypass the limitation caused by grain boundaries.

Because the production of high quality graphene remains a significant challenge, the use of graphene as TCEs in organic solar cells is still at its infant stage [143, 144]. Only a few proof-of-concept studies have been completed that use graphene in dye sensitized or small molecule solar cells. To date, the performance of these cells has been limited (e.g. PCEs < 1 %) [145] due to the high sheet resistance of the films, often in the thousands of ohm square range [146]. De Arco et al. used CVD to apply an optimized graphene film with an R_s of $3500 \Omega/\text{sq}$ and $T=89\%$ to successfully demonstrate a small molecule solar cell with a PCE of 1.18 % [147]. These results affirm that in order for graphene films to become a viable candidate for ITO replacement, a low-cost fabrication process must be developed that further reduces sheet resistance.

A variety of approaches have been developed to reduce sheet resistance in graphene films. For example, multiple layers of graphene made by repeated transfer techniques can result in a sheet resistance of as low as $80\ \Omega/\text{sq}$ with a $T=90\%$ (550 nm) [148]. Choe et al. used high quality CVD-grown multilayer graphene films (15 layers) and make P3HT:PCBM-based OPVs with a PCE of 2.6% [149]. Chemical doping of graphene with AlCl_3 is another way to improve the conductivity of graphene; this approach has been shown to reduce sheet resistance by 77% with only 2% decrease in transmission. Kim et al. reported an improvement in PCE 1.63% for AlCl_3 -doped graphene film in comparison of PCE 1.36% for undoped graphene on OPV devices [150].

6.4 Hybrid Materials-Based Alternative TCEs

As described above, the sheet resistance of TCEs made from any stand-alone inorganic, organic or nanomaterial still remains significantly higher than that of commercial ITO ($10\text{--}60\ \Omega/\text{sq}$) and thus yields lower PCEs than ITO-based devices. Another approach to further improving the conductivity of alternative TCEs is to use a combination of multiple types of conducting materials, such as PEDOT:PSS, CNTs, metal grids and nanowires and graphene. For example, replacing ITO with a composite electrode made from hybrid materials in a regular geometry solar cell resulted in a multi-fold decrease in series resistance compared to the use of a single conducting component, ultimately resulting in a several-fold increase in efficiency [31]. Galagan et al. reported the integration of a R2R-produced composite electrode into an OPV. The device included embedded current collecting silver grids combined with highly conductive PEDOT:PSS [32]. The resulting flexible OPV devices enabled by these hybrid electrodes have significantly improved efficiencies over large areas ($4\ \text{cm}^2$) compared to ITO-based devices. Experimental measurements show much higher PCE ($>2\%$) than identical flexible devices fabricated using ITO ($\sim 1\%$) and inkjet-printed silver ($\sim 1.5\%$). This is mainly due to the much lower sheet resistance that results from the embedded Ag grid structure. Since the efficiency of devices decreases with increasing sheet resistance, the lower sheet resistance of PEDOT:PSS/Ag grid in comparison to inkjet printed Ag and ITO ($0.21\ \Omega/\text{sq}$ vs. $4.83\ \Omega/\text{sq}$ and $60\ \Omega/\text{sq}$, respectively) opens up the potential for producing large area OPV devices with greater process and design freedom.

6.4.1 PEDOT:PSS-Metal-Based Hybrid TCEs

Krebs et al. compared the performance of embedded Ag grids with that of flexographic printed Ag grids when used in conjunction with highly conducting PEDOT:PSS. Both materials were assembled to form semitransparent, ITO-free front electrodes for use in polymer solar cells. Results demonstrated that both topographies work equally well. When large area devices ($6\ \text{cm}^2$) were tested outdoors by exposure to

the sun, the PCE obtained for thermally imprinted, inkjet and flexographic Ag grids was found to be 1.84, 0.79 and 1.72 %, respectively. While the flexographic grid enabled the fastest processing, the smallest use of Ag, and the best topography, the embedded grid achieved the best optical transparency and conductivity [151]. One challenge of using hybrid electrodes achieving an optimal balance between shadow losses due to the metal grids and the resistive losses due to the high resistance of the combined PEDOT:PSS/metal electrode. To minimize the loss of incoming light exposure on the photoactive layer, the surface coverage of the metal grids should be as small as possible. Kang et al. demonstrated that the surface coverage can be minimized while maintaining the conductivity by increasing the grid line height [152]. Depending on the conductivity grade of PEDOT:PSS, different metal grid configurations must be optimized to achieve the best PCE. This can include grid spacing, width and height [43, 45]. Na et al. used ink-jet-printed current collecting Ag grids in combination with highly conductive PEDOT:PSS to obtain a transparent composite electrode with a sheet resistance of 15.8 Ω/sq . and optical transmittance of 82.5 % at 550 nm wavelength. An ITO-free OPV device fabricated using these hybrid materials to form a transparent anode on a flexible substrate exhibited excellent cell-performances: FF of ~ 65 %, short-circuit current density of 6.3 mA cm^{-2} , open-circuit voltage of 0.56 V and PCE of 2.3 % [153].

Silver grids are not the only materials that can be integrated with a PEDOT:PSS electrode to reduce resistive power loss. Kippelen et al. fabricated an ITO-free large-area device (7.3 cm^2) by sputtering a thin layer of Au (100 nm) onto a thick layer of electroplated Cu (5 μm). The thin Au grid connects the PEDOT:PSS electrode to the thick Cu grid. This device yielded a PCE of 0.7 %, comparable to a similarly-sized, ITO-based device that achieved a PCE of 0.8 % [154]. Kim et al also reported a highly clear conductive polymer electrode film comprised of PEDOT:PSS and gold nanoparticles. The gold nanoparticles increased conductivity of the hybrid film seven-fold compared to that of the PEDOT:PSS alone [155].

Similarly, Ag NWs-PEDOT:PSS has been used to demonstrate cost-effective ITO-free OPVs. In this approach, composite Ag NWs-PEDOT:PSS films can be either prepared with a one-step spray-coating of a mixture of composed of Ag NWs and DMSO-treated PEDOT:PSS or a two-step spraying of individual component in sequence. The film-thickness, optical transmittance and sheet resistance of Ag NWs-PEDOT:PSS hybrid electrodes can be easily controlled by varying the spray deposition time. As shown in Fig. 6.17, spray-coated PEDOT:PSS performs two functions: (1) adhesion promotion of the Ag NWs to the substrate; thus overcoming the generally weak adhesion between nanowire and substrates [156]; (2) surface roughness reduction, resulting in reduced shorting and improved cell-efficiency. Ag NWs embedded in PEDOT:PSS consolidate the nanowire contacts to enhance conductivity of the overall film. Under room temperature processing conditions, Choi et al. fabricated a Ag NWs-PEDOT:PSS composite film that showed a 10.8 Ω/sq sheet resistance with $T=84$ %. More remarkably, the sheet resistance of the composite film only slightly increased during 200 cycles of compression and folding, demonstrating great potential for future flexible optoelectronic applications [157].

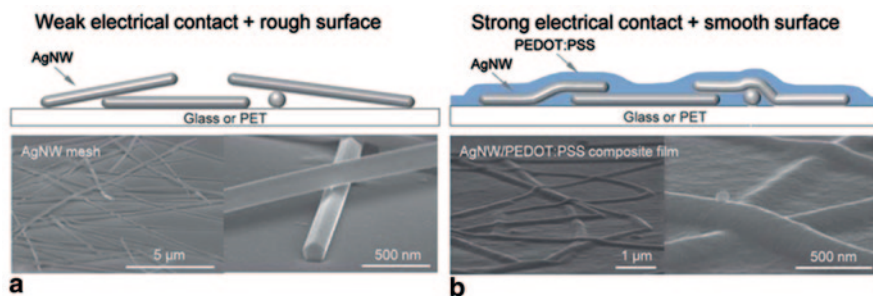


Fig. 6.17 Schematic diagram showing the roles of PEDOT:PSS in reducing the surface roughness and improving the electrical contact. **a** Bare Ag NWs mesh, **b** Ag NWs-PEDOT:PSS composite film. (Reprinted with permission from Ref. [157], copyright The Royal Society of Chemistry 2013)

6.4.2 PEDOT:PSS-CNTs-Based Hybrid TCEs

Flexible transparent electrodes can also be formed by embedding CNTs in a variety of different polymers, including PEDOT:PSS [158, 159], polyaniline (PANI) [160], or polyimide [161]. Bardeen's group demonstrated the ability to control the placement of a SWCNT monolayer network at different positions in polymer-fullerene bulk heterojunction solar cells. To achieve this, the researchers used a brief, largely non-destructive argon plasma treatment of the photoactive layer. It was shown that the incorporation of SWCNTs on the hole-collection side of the photoactive layer increases the PCE of the OPV devices from 4 to 4.9% under 1.3 suns illumination, resulting in one of the highest reported PCEs for a polymer-based solar cell incorporating CNTs [162]. Simple print-based fabrication methods have also been developed to make low cost TCEs. For example, Cho et al. brush-painted hybrid PEDOT:PSS/CNTs materials on flexible PET and achieved percolated CNT network electrodes with a low-sheet resistance of 286 Ω/sq and a high diffusive transmittance of 78.45% with a superior mechanical flexibility. The electrical, optical and mechanical properties of the resulting electrodes were shown to be a function of the number of repeated brush-painting cycles. Optimized OPV devices fabricated on such hybrid material-based TCEs showed a PCE \sim 1.6% [163].

6.4.3 Graphene and GO-Based Hybrid TCEs

The conductivity of solution-processed graphene films can be improved by incorporating conductive filler materials. For example, recent reports have shown the benefit of incorporating CNTs into a matrix of graphene. Tung et al. mixed GO and CNTs in anhydrous hydrazine and spin-coated the mixture onto glass substrates. After p-doping with SOCl_2 , the TCE presented a sheet resistance of 240 Ω/sq with $T=86\%$ [164]. Another hybrid film consisting of CNT and CVD graphene achieved a sheet resistance of 735 Ω/sq with $T=90\%$. When used as the top electrode in a Si-based solar cell, the hybrid film enabled a record high PCE of 5.2% [165].

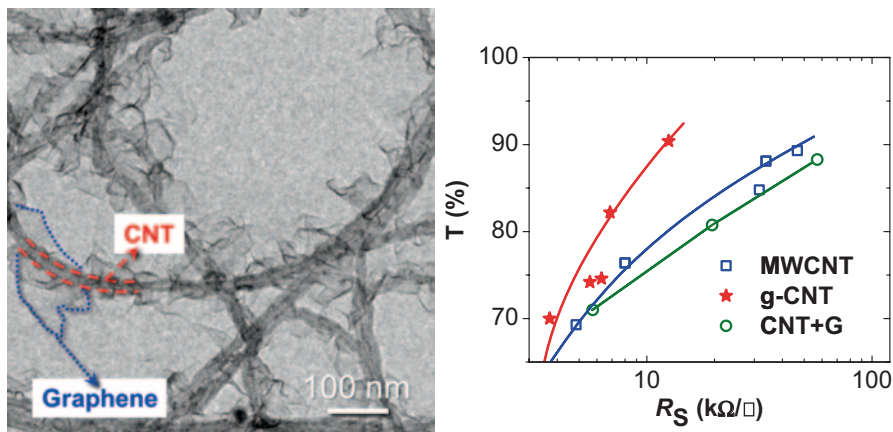


Fig. 6.18 *Left*: TEM image of graphenated CNT (g-CNT); *Right*: its improvement on T% versus R_s compared with a physical mixture of graphene and CNT. (Reprinted with permission from Ref. [167], copyright 2011 American Chemical Society)

Although it is generally believed that both the graphene and the CNTs (or other filler material) offer conduction pathways in a percolation network, the mechanism of mixing is still under debate since additional tube-flake junction resistance can be introduced. A study argued that the addition of graphene into a SWCNT network cannot improve the property of the hybrid TCEs unless it is SOCl_2 doped [166]. Chen et al. have reported that covalently-bonded CNT and graphene hybrid material (g-CNT), in which the graphene grown on the sidewall of a CNT with a plasma-enhanced chemical vapour deposition as shown in Fig. 6.18, can minimize such a tube-flake junction resistance with an increase on transmittance [167, 168]. Huang's group has reported that water-processable GO:SWCNTs thin films can replace PEDOT:PSS as an effective interfacial layer to construct tandem polymer solar cells in both regular and inverted geometry by solution processing routes. Such a GO:SWCNTs thin film serve as good mechanical separator and electric interconnect and has significantly increased open-circuit voltage and improved PCEs [169, 170].

Similarly, high-performance hybrid TCEs can be made by combining graphene and metallic nanowires or grids. The advantages of this approach are many: for example, a solution processable Ag NWs/rGO hybrid transparent electrode has high optical transmittance and low-sheet resistance, which is comparable to ITO transparent electrode in OPV devices. The rGO layer can dissipate heat and electrical stress, and thus provides resistance against electrical breakdown. In addition, it has been found that these types of hybrid TCEs exhibit highly enhanced thermal and chemical stabilities due to the excellent gas-barrier property, because of passivation layer formed by rGO on Ag NW films [171]. Another report shows that a Ag NW-graphene film exhibits an excellent properties ($33 \Omega/\text{sq}$, $T=94\%$ at 550 nm) due to the high intrinsic conductivity of the Ag NW network [172]. When Kim et al. fabricated hybrid transparent conductive films consisting of multilayer graphene

and metal grids, they achieved a sheet resistance of as low as $\sim 20 \Omega/\text{sq}$ with an optical transmittance of 87% at 550 nm. The device characteristics of OPVs prepared on hybrid films include an open circuit voltage of 0.58 V, a short circuit current of $8.05 \text{ mA}/\text{cm}^2$, a FF of 51%, and a PCE of 2.4%. Compared with that of OPVs fabricated using multilayer graphene films without Ag grids, the improvement on PCE can be attributed to the reduced sheet resistance of the hybrid film [173].

6.5 Outlook

Table 6.2 summarizes the properties of alternative TCE materials mentioned in this chapter when compared to ITO. We hope that our review reflects the vitality of current research on alternative TCE materials. As consumer optoelectronic devices become increasingly more ubiquitous, the demand for better and cheaper TCE materials will continue to grow. Will alternative TCEs eventually replace ITO? Although it is impossible to predict the future, significant progress has been made in the last few years to improve the properties of alternative TCE materials. The result has been a rapid increase in reliability and stability, and a reduction in defects and cost. Undoubtedly, the electronics industry will be the initial beneficiary of the progress in these research areas. The similarity in the fundamental processes between light display and energy conversion devices means that improved organic solar cell devices will likely follow. Indeed, a recent innovation that enables the use of perovskite solar cell research may spark further improvement in TCEs. This approach uses a low-cost, solution-based deposition procedure utilizing nanocomposites of graphene and TiO_2 nanoparticles as the electron collection layers. The resulting meso-superstructured perovskite solar cells showed remarkable photovoltaic performance, achieving a record PCE of 15.6% [174]. Other promising approaches include PECVD [175, 176] and catalyst-free growth [177] techniques that enable low-temperature ($400\text{--}650^\circ\text{C}$), direct growth of graphene on dielectric substrates SiO_2/Si . Methods such as these that are compatible with the existing infrastructure of the semiconductor industry will undoubtedly have an advantage over those that use non-conventional manufacturing approaches. The high degree of initial success and continued rapid progress of CNT, graphene, nanowire and organic conducting polymer technology, suggests that it will not be too long before these materials are utilized in the fabrication of a commercial replacement for ITO for broad use in optoelectronics and organic solar cells in particular.

Table 6.2 Summary of the properties of alternative TCE materials comparing to ITO

Materials	Conductivity	Transparency	Printability	Flexibility	Stretchability	Stability	Commercial suppliers
ITO	Good	Excellent	Poor	Poor	Poor	Excellent	Multek Delta Technologies
Ag Grid	Excellent	Good	Good	Good	Poor	Excellent	Cabot Pchem
Ag NWs	Excellent	Poor	Good	Good	Poor	Excellent	Cambrios Carestream
PEDOT:PSS	Poor	Excellent	Excellent	Excellent	Excellent	Poor	Agfa Heraeus
CNT	Poor	Excellent	Excellent	Excellent	Excellent	Good	SWeNT Linde
Graphene	Good	Excellent	Excellent	Excellent	Excellent	Poor	Graphenea Graphene Platform

References

1. Tang, C. W., *Appl. Phys. Lett.* 1986, 48, 183.
2. Sheraw, C. D.; Zhou, L.; Huang, J. R.; Gundlach, D. J.; Jackson, T. N.; Kane, M. G.; Hill, I. G.; Hammond, M. S.; Campi, J.; Greening, B. K., *Appl. Phys. Lett.* 2002, 80, 1088.
3. Tak, Y.; Kim, K.; Park, H.; Lee, K.; Lee, J., *Thin Solid Films* 2002, 411, 12.
4. Madaria, A. R.; Kumar, A.; Zhou, C., *Nanotechnology* 2011, 22, 245201.
5. Granqvist, C. G.; Hultaker, A., *Thin Solid Films* 2002, 411, 1.
6. Wang, L.; Yoon, M.; Lu, G.; Yang, Y.; Facchetti, A.; Marks, T. J., *Nature Materials* 2006, 5, 893.
7. Andersson, A.; Johansson, N.; Broems, P.; Yu, N.; Lupo, D.; Salaneck, W. R. *Adv. Mater.* 1998, 10, 859.
8. Miyata, T.; Ohtani, Y.; Kuboi, T.; Minami, T., *Thin Solid Films* 2008, 516, 1354.
9. Formica, N.; Ghosh, D. S.; Martinez-Otero, A.; Chen, T. L.; Martorell, J.; Pruneri, V., *Appl. Phys. Lett.* 2013, 103, 183304.
10. Hecht, D. S.; Hu, L.; Irvin, G., *Adv. Mater.* 2011, 13, 1482.
11. Kumar, A.; Zhou, C., *ACS Nano* 2010, 1, 11.
12. Sun, Y.; Rogers, J. A., *Adv. Mater.* 2007, 15, 1897.
13. Dou, L.; You, J.; Hong, Z.; Xu, Z.; Li, G.; Street, R. A.; Yang, Y., *Adv. Mater.* 2013, 25, 6642.
14. Ryuzaki, S.; Onoe, J., *Nano Reviews* 2013, 4, 21055.
15. Emmott, C. J. M.; Urbina, A.; Nelson, J., *Sol. Energy Mater. Sol. Cells* 2012, 97, 14.
16. Azzopardi, B.; Emmott, C. J. M.; Urbina, A.; Krebs, F. C.; Mutale, J.; Nelson, J. *Energy Environ. Sci.* 2011, 4, 3741.
17. Huebler, A. C.; Kempa, H., Edited by Brabec; Dyakonov, V.; Scherf, U., *Organic Photovoltaics* 2008, 513–529.
18. Li, Y. Q.; Tang, J. X.; Xie, Z. Y.; Hung, L. S.; Lau, S. S., *Chem. Phys. Lett.* 2004, 386, 128.
19. Pode, R. B.; Lee, C. J.; Moon, D. G.; Han, J. I., *Appl. Phys. Lett.* 2004, 84, 4614.
20. O'Connor, B.; An, K. H.; Pipe, K. P.; Zhao, Y.; Shtein, M., *Appl. Phys. Lett.* 2006, 89, 233502.
21. Oyamada, T.; Sugawara, Y.; Terao, Y.; Sasabe, H.; Adachi, C., *Jpn. J. Appl. Phys., Part I* 2007, 46, 1734.
22. Klauk, H.; Huang, J. R.; Nichols, J. A.; Jackson, T. N., *Thin Solid Films* 2000, 366, 272.
23. Krebs, F. C., *Sol. Energy Mater. Sol. Cells* 2009, 93, 394.
24. Søndergaard, R.; Høsel, M.; Angmo, D.; Larsen-Olsen, T. T.; Krebs, F. C., *Mater. Today* 2012, 15, 36.
25. Maillaud, L.; Zakri, C.; Ly, I.; Penicaud, A.; Poulin, P., *Appl. Phys. Lett.* 2013, 103, 263106.
26. Chien, Y.; Izquierdo, R., Edited by Morris; Iniewski, K., *Graphene, Carbon Nanotubes, and Nanostructures* 2013, 61–87.
27. Park, S.; Vosguerichian, M.; Bao, Z., *Nanoscale* 2013, 5, 1727.
28. Verma, V. P.; Das, S.; Lahiri, I.; Choi, W., *Appl. Phys. Lett.* 2010, 96, 203108.
29. Hecht, D. S.; Kaner, R. B. *MRS Bulletin* 2011, 36, 749.
30. Lian, W.; Huang, Y.; Liao, Y.; Wang, K.; Li, L.; Su, C.; Liaw, D.; Lee, K.; Lai, J., *Macromolecules* 2011, 44, 9550.
31. Hoesel, M.; Søndergaard, R. R.; Jorgensen, M.; Krebs, F. C. *Energy Technology* 2013, 1, 102.
32. van de Wiel, H. J.; Galagan, Y.; van Lammeren, T. J.; de Riet, J. F. J.; Gilot, J.; Nagelkerke, M. G. M.; Lelieveld, R. H.; Shanmugam, S.; Pagudala, A.; Hui, D., *Nanotechnology* 2013, 24, 484014.
33. De, S.; Coleman, J. N., *ACS Nano* 2010, 5, 2713.
34. Eritt, M.; May, C.; Leo, K.; Toerker, M.; Radehaus, C., *Thin Solid Films* 2010, 11, 3042.
35. Pankove, J. I., *Optical Processes in Semiconductors Chapter 1*. Dover 1971.
36. Bubnova, O.; Khan, Z. U.; Malti, A.; Braun, S.; Fahlman, M.; Berggren, M.; Crispin, X., *Nature Materials* 2011, 10, 429.
37. Ellmer, K., *Nature Photon.* 2012, 12, 809.
38. Nair, R. R.; Blake, P.; Grigorenko, A. N.; Novoselov, K. S.; Booth, T. J.; Stauber, T.; Peres, N. M. R.; Geim, A. K., *Science* 2008, 5881, 1308.

39. Bernède, J. C.; Berredjem, Y.; Cattin, L.; Morsli, M., *Appl. Phys. Lett.* 2008, 92, 083304.
40. Mapel, J. K.; Singh, M.; Baldo, M. A.; Celebi, K., *Appl. Phys. Lett.* 2007, 90, 121102.
41. O'Connor, B.; Haughn, C.; An, K.; Pipe, K. P.; Shtein, M., *Appl. Phys. Lett.* 2008, 93, 223304.
42. Angmo, D.; Høsel, M.; Krebs, F. C., *Sol. Energy Mater. Sol. Cells* 2012, 107, 329.
43. Tvingstedt, K.; Inganäs, O., *Adv. Mater.* 2007, 19, 2893.
44. Galagan, Y.; Zimmermann, B.; Coenen, E. W. C.; Jørgensen, M.; Tanenbaum, D. M.; Krebs, F. C.; Gortler, H.; Sabik, S.; Slooff, L. H.; Veenstra, S. C.; Kroon, J. M.; Andriessen, R., *Adv. Energy Mater.* 2012, 2103.
45. Galagan, Y.; Rubingh, J. J. M.; Andriessen, R.; Fan, C.; Blom, P. W. M.; Veenstra, S. C.; Kroon, J. M. *Sol. Energy Mater. Sol. Cells* 2011, 95, 1339.
46. He, P.; Gu, C.; Cui, Q.; Guo, X., *Proc. SPIE* 2011, 8312, 83120A1
47. Layani, M.; Magdassi, S., *J. Mater. Chem.* 2011, 21, 15378.
48. Hau, S. K.; Yip, H.; Leong, K.; Jen, A. K.-Y., *Organic Electronics* 2009, 10, 719.
49. Lee, S.-H.; Shin, K.-Y.; Hwang, J. Y.; Kang, K. T.; Kang, H. S., *J. Micromech. Microeng.* 2008, 18, 075014
50. Meier, H.; Löffelmann, U.; Mager, D.; Smith, P. J.; Korvink, J. G., *Phys. Status Solidi A* 2009, 206, 1626.
51. R. Shankar, L. Groven, A. Amert, K. W. Whites, J. J. Kellar, *J. Mater. Chem.* 2011, 21, 10871.
52. J. Perelaer, P. J. Smith; D. Mager; D. Soltman; S. K. Volkman; V. Subramanian; J. G. Korvink; U. S. Schubert, *J. Mater. Chem.* 2010, 20, 8446.
53. Y. Wu, Y. Li, B. S. Ong, *J. Am. Chem. Soc.* 2006, 128, 4202.
54. S. F. Jahn, A. Jakob, T. Blaudeck; P. Schmidt; H. Lang; R. R. Baumann, *Thin Solid Films* 2010, 518, 3218.
55. Y. Wu, Y. Li, B. Ong, *J. Am. Chem. Soc.* 2007, 129, 1862.
56. S.-P. Chen, Z.-K. Kao, J.-L. Lin, Y.-C. Liao, *ACS Appl. Mater. Interfaces* 2012, 4, 7064.
57. S. B. Walker; J. A. Lewis, *J. Am. Chem. Soc.* 2012, 134, 1419.
58. B. Y. Ahn, D. J. Lorange, J. A. Lewis, *Nanoscale* 2011, 3, 2700.
59. S. B. Walker, B. Y. Ahn, J. A. Lewis, *Material Matters* 2014, 9, 1.
60. Galagan, Y.; Coenen, E. W. C.; Sabik, S.; Gortler, H. H.; Barink, M.; Veenstra, S. C.; Kroon, J. M.; Andriessen, R.; Blom, P. W. M., *Sol. Energy Mater. Sol. Cells* 2012, 104, 32.
61. Sun, Y.; Gates, B.; Mayers, B. T.; Xia, Y., *Nano Lett.* 2002, 2, 165.
62. Lim, J. -W.; Cho, D. -Y.; Kim, J.; Na, S. -I.; Kim, H. -K., *Sol. Energy Mater. Sol. Cells* 2012, 107, 348.
63. De, S.; Higgins, T. M.; Lyons, P. E.; Doherty, E. M.; Nirmalraj, P. N.; Blau, W. J.; Boland, J. J.; Coleman, J. N., *ACS Nano* 2009, 3, 1767.
64. Lee, J.; Connor, S. T.; Cui, Y.; Peumans, P., *Nano Lett.* 2008, 8, 689.
65. A. Tao, P. Sinsermsuksakul, P. D. Yang, *Angew. Chem. Int. Ed.* 2006, 45, 4597.
66. Pradel, K. C.; Sohn, K.; Huang, J., *Angew. Chem. Int. Ed.* 2011, 123, 3474.
67. Yang, L.; Zhang, T.; Zhou, H.; Price, S. C.; Wiley, B. J.; You, W., *ACS Appl. Mater. Interfaces* 2011, 3, 4075.
68. Gaynor, W.; Burkhard, G. F.; McGehee, M. D.; Peumans, P., *Adv. Mater.* 2011, 23, 2905.
69. Leem, D.; Edwards, A.; Faist, M.; Nelson, J.; Bradley, D. D. C.; de Mello, J. C., *Adv. Mater.* 2011, 23, 4371.
70. Ajuria, J.; Ugarte, I.; Cambarau, W.; Etxebarría, I.; Tena-Zaera, R.; Pacios, R., *Sol. Energy Mater. Sol. Cells* 2012, 102, 148.
71. Morgenstern, F. S. F.; Kabra, D.; Massip, S.; Brenner, T. J. K.; Lyons, P. E.; Coleman, J. N.; Friend, R. H., *Appl. Phys. Lett.* 2011, 99, 183307.
72. Stubhan, T.; Krantz, J.; Li, N.; Guo, F.; Litzov, I.; Steidl, M.; Richter, M.; Matt, G. J.; Brabec, C. J., *Sol. Energy Mater. Sol. Cells* 2012, 107, 248–251.
73. Madaria, A. R.; Kumar, A.; Ishikawa, F. N.; Zhou, C., *Nano Res.* 2010, 3, 564.
74. Tokuno, T.; Nogi, M.; Karakawa, M.; Jiu, J.; Thi Thi Nge; Aso, Y.; Suganuma, K. *Nano Res.* 2011, 4, 1215.
75. R. Zhu, C. Y. Jiang, X. Z. Liu and B. Liu, *Appl. Phys. Lett.* 2008, 93, 013102.

76. Jiu, J.; Sugahara, T.; Nogi, M.; Araki, T.; Suganuma, K.; Uchida, H.; Shinozaki, K., *Nanoscale* 2013, 5, 11820.
77. Coskun, S.; Ates, E. S.; Unalan, H. E., *Nanotechnology* 2013, 24, 125202.
78. Wu, J.; Hsu, S. L.; Tsai, M.; Liu, Y.; Hwang, W., *J. Mater. Chem.* 2012, 22, 15599.
79. Spechler, J. A.; Arnold, C. B., *Appl. Phys. A* 2012, 108, 25.
80. Guo, F.; Zhu, X.; Forberich, K.; Krantz, J.; Stubhan, T.; Salinas, M.; Halik, M.; Spallek, S.; Butz, B.; Spiecker, E., *Adv. Eng. Mater.* 2013, 3, 1062.
81. Hauger, T. C.; Al-Rafia, S. M. I.; Buriak, J. M., *ACS Applied Materials & Interfaces* 2013, 5, 12663.
82. Scardaci, V.; Coull, R.; Coleman, J. N., *IEEE International Conference on Nanotechnology, 12th*, Birmingham, United Kingdom, 2012, 214–216.
83. <http://www.cambrios.com/opv>
84. <http://www.carestream.com/specials/adv-materials/products.html>
85. Fuh, Y. -K.; Lien, L. -C., *Nanotechnology* 2013, 24, 055301.
86. Krebs, F.C.; Tromholt, T.; Jorgensen, M., *Nanoscale* 2010, 2, 873.
87. Krebs, F.C.; Nielsen, T.D.; Fyenbo, J.; Wadstrom, M.; Pedersen, M.S., *Energy Environ. Sci.* 2010, 3, 512.
88. Kirchmeyer, S.; Reuter, K., *J. Mater. Chem.* 2005, 15, 2077.
89. Levermore, P. A.; Chen, L.; Wang, X.; Das, R.; Bradley, D. D. C. *Adv. Mater.* 2007, 19, 2379.
90. Groenendaal, B. L.; Jonas, F.; Freitag, D.; Pielartzik, H.; Reynolds, J. R., *Adv. Mater.* 2000, 12, 481.
91. Winther-Jensen, B.; Krebs, F. C., *Sol. Energy Mater. Sol. Cells* 2006, 90, 123.
92. Hsiao, Y.; Whang, W.; Chen, C.; Chen, Y., *J. Mater. Chem.* 2008, 18, 5948.
93. Ouyang, B. Y.; Chi, C. W.; Chen, F. C.; Xi, Q. F.; Yang, Y., *Adv. Funct. Mater.* 2005, 15, 203.
94. Zhang, F. L.; Johansson, M.; Andersson, M. R.; Hummelen, J. C.; Inganäs, O., *Adv. Mater.* 2002, 14, 662.
95. Ahlswede, E.; Hanisch, J.; Powalla, M., *Appl. Phys. Lett.* 2007, 90, 163504.
96. Na, S.; Kim, S.; Jo, J.; Kim, D. *Adv. Mater.* 2008, 20, 4061.
97. Zhang, X. G.; Butler, W. H., *Phys. Rev. B* 1995, 51, 10085.
98. Krebs, F.C., *Polymeric Solar Cells: Materials, Design, Manufacture*. DEStech Publications, Inc., Lancaster, Pennsylvania, 2010.
99. <http://aldrich.com/matsci>
100. Gilot, J.; Wienk, M. M.; Janssen, R. A., *Adv. Mater.* 2010, 22, E67
101. Iijima, S., *Nature* 1991, 354, 56.
102. Shim, B. S.; Tang, Z.; Morabito, M. P.; Agarwal, A.; Hong, H.; Kotov, N. A., *Chem. Mater.* 2007, 19, 5467.
103. Tans, S.J.; Devoret, H.; Thess, A.; Smalley, R.E.; Geerligs, L.J.; Dekker, C., *Nature* 1997, 386, 474.
104. Meo, M.; Rossi, M., *Composite Science and Technology* 2006, 66, 1597.
105. Wu, Z. C.; Chen, Z. H.; Du, X.; Logan, J. M.; Sippel, J.; Nikolou, M.; Kamaras, K.; Reynolds, J. R.; Tanner, D. B.; Hebard, A. F.; Rinzler, A. G., *Science* 2004, 305, 1273.
106. J. L. Blackburn, T. M. Barnes, M. C. Beard, Y.-H. Kim, R. C. Tenent, T. J. McDonald, B. To, T. J. Coutts and M. J. Heben, *ACS Nano* 2008, 2, 1266.
107. K. S. Mistry, B. A. Larsen, J. D. Bergeson, T. M. Barnes, G. Teeter, C. Engtrakul and J. L. Blackburn, *ACS Nano* 2011, 5, 3714.
108. Arnold, M.; Green, A.; Hulvat, J.; Stupp, S.; Hersam, M., *Nature Nanotechnology* 2006, 1, 60.
109. T. M. Barnes, J. L. Blackburn, J. van de Lagemaat, T. J. Coutts and M. J. Heben, *ACS Nano* 2008, 2, 1968.
110. Coakley, K. M.; McGehee, M. D., *Chem. Mater.* 2004, 16, 4533.
111. Rowell, M. W.; Topinka, M. A.; McGehee, M. D.; Prall, H.; Dennler, G.; Sariciftci, N. S.; Hu, L.; Gruner, G., *Appl. Phys. Lett.* 2006, 88, 233506.
112. Kim, S.; Yim, J.; Wang, X.; Bradley, D. D. C.; Lee, S.; deMello, J. C., *Adv. Funct. Mater.* 2010, 20, 2310.

113. Kim, S.; Wang, X.; Yim, J. H.; Tsoi, W. C.; Kim, J.; Lee, S.; deMello, J. C., *J. Photonics Energy* 2012, 2, 021010.
114. H. Ago, K. Petritsch, M. S. P. Shaffer, A. H. Windle, and R. H. Friend, *Adv. Mater.* 1999, 11, 1281.
115. Ulbricht, R.; Lee, S. B.; Jiang, X.; Inoue, K.; Zhang, M.; Fang, S.; Baughman, R. H.; Zakhidov, A. A., *Sol. Energy Mater. Sol. Cells* 2007, 91, 416.
116. Mayorov, A. S.; Gorbachev, R. V.; Morozov, S. V.; Britnell, L.; Jalil, R.; Ponomarenko, L. A.; Blake, P.; Novoselov, K. S.; Watanabe, K.; Taniguchi T.; Geim, A. K., *Nano Lett.* 2011, 11, 2396.
117. Balandin, A. A.; Ghosh, S.; Bao, W.; Calizo, I.; Teweldebrhan, D.; Miao, F.; Lau, C. N., *Nano Lett.* 2008, 8, 902.
118. Lee, C.; Wei, X. D.; Kysar J. W.; Hone, J., *Science* 2008, 321, 385.
119. Geim, A. K.; Novoselov, K. S., *Nat. Mater.* 2007, 6, 183.
120. Bonaccorso, F.; Sun, Z.; Hasan, T.; Ferrari, A. C., *Nat. Photonics* 2010, 4, 611.
121. Wu, J.; Agrawal, M.; Becerril, H. A.; Bao, Z.; Liu, Z.; Chen, Y.; Peumans, P., *ACS Nano* **2009**, 1, 43.
122. Yu, K.; Chen, H., *Material Matters* 2014, 9, 1.
123. Reina, A.; Jia, X.; Ho, J.; Nezich, D.; Son, H.; Bulovic, V.; Dresselhaus, M. S.; Kong, J., *Nano Lett.* 2008, 1, 30.
124. Tenent, R. C.; Barnes, T. M.; Bergeson, J. D.; Ferguson, A. J.; To, B.; Gedvilas, L. M.; Heben, M. J.; Blackburn, J. L., *Adv. Mater.* 2009, 21, 3210.
125. Kim, K. S.; Zhao, Y.; Jang, H.; Lee, S. Y.; Kim, J. M.; Kim, K. S.; Ahn, J.-H.; Kim, P.; Choi, J.-Y.; Hong, B. H., *Nature* 2009, 7230, 706.
126. Li, X.; Zhu, Y.; Cai, W.; Borysiak, M.; Han, B.; Chen, D.; Piner, R. D.; Colombo, L.; Ruoff, R. S., *Nano Lett.* 2009, 12, 4359.
127. Mattevi, C.; Kim, H.; Chhowalla, M., *J. Mater. Chem.* 2011, 10, 3324.
128. Zhang, Y.; Zhang, L.; Zhou, C., *Acc. Chem. Res.* 2013, 10, 2329.
129. Chen, Y. P.; Yu, Q.; Newell, D.; Wu, W.; Jauregui, L. A.; Cao, H.; Shen, T.; Chung, T. F., *Int. J. Mod. Phys. B* 2013, 10, 1341002.
130. Bae, S.; Kim, H.; Lee, Y.; Xu, X.; Park, J.-S.; Zheng, Y.; Balakrishnan, J.; Lei, T.; Ri Kim, H.; Song, Y. I.; Kim, Y.-J.; Kim, K. S.; Ozyilmaz, B.; Ahn, J.-H.; Hong, B. H.; Iijima, S., *Nature Nanotech.* 2010, 8, 574.
131. Becerril, H. A.; Mao, J.; Liu, Z.; Stoltenberg, R. M.; Bao, Z.; Chen, Y., *ACS Nano* 2008, 3, 463.
132. Wang, J.; Liang, M.; Fang, Y.; Qiu, T.; Zhang, J.; Zhi, L., *Adv. Mater.* 2012, 21, 2874.
133. Eda, G.; Fanchini, G.; Chhowalla, M., *Nature Nanotech.* 2008, 5, 270.
134. Li, X.; Zhang, G.; Bai, X.; Sun, X.; Wang, X.; Wang, E.; Dai, H., *Nature Nanotech.* 2008, 9, 538.
135. Zhao, J.; Pei, S.; Ren, W.; Gao, L.; Cheng, H.-M., *ACS Nano* 2010, 9, 5245.
136. Mao, S.; Pu, H.; Chen, J., *RSC Adv.* 2012, 7, 2643.
137. Mattevi, C.; Eda, G.; Agnoli, S.; Miller, S.; Mkhoyan, K. A.; Celik, O.; Mastrogiovanni, D.; Granozzi, G.; Garfunkel, E.; Chhowalla, M., *Adv. Funct. Mater.* 2009, 16, 2577.
138. Eda, G.; Lin, Y.-Y.; Miller, S.; Chen, C.-W.; Su, W.-F.; Chhowalla, M., *Appl. Phys. Lett.* 2008, 92, 233305.
139. Hernandez, Y.; Nicolosi, V.; Lotya, M.; Blighe, F. M.; Sun, Z.; De, S.; McGovern, I. T.; Holland, B.; Byrne, M.; Gun'Ko, Y. K.; Boland, J. J.; Niraj, P.; Duesberg, G.; Krishnamurthy, S.; Goodhue, R.; Hutchison, J.; Scardaci, V.; Ferrari, A. C.; Coleman, J. N., *Nature Nanotech.* 2008, 9, 563.
140. Green, A. A.; Hersam, M. C., *Nano Lett.* 2009, 12, 4031.
141. Blake, P.; Brimicombe, P. D.; Nair, R. R.; Booth, T. J.; Jiang, D.; Schedin, F.; Ponomarenko, L. A.; Morozov, S. V.; Gleeson, H. F.; Hill, E. W.; Geim, A. K.; Novoselov, K. S., *Nano Lett.* 2008, 6, 1704.
142. Jo, G.; Choe, M.; Lee, S.; Park, W.; Kahng, Y. H.; Lee, T., *Nanotechnology* 2012, 23, 112001.
143. Iwan, A.; Chuchmala, A., *Progress in Polymer Science* 2012, 37, 1805.

144. Wu, J.;Becerril, H. A.;Bao, Z.;Liu, Z.;Chen, Y.;Peumans, P., *Appl. Phys. Lett.* 2008, 92, 263302.
145. Wang, X.;Zhi, L.;Muellen, K., *Nano Lett.* 2008, 8, 323.
146. De Arco, L. G.;Zhang, Y.;Schlenker, C. W.;Ryu, K.;Thompson, M. E.;Zhou, C., *ACS Nano* 2010, 4, 2865.
147. Wang, Y.;Tong, S. W.;Xu, X. F.;Ozyilmaz, B.;Loh, K. P., *Adv. Mater.* 2011, 23, 1514.
148. Choe, M.;Lee, B. H.;Jo, G.;Park, J.;Park, W.;Lee, S.;Hong, W.;Seong, M.;Kahng, Y. H.;Lee, K.;Lee, T., *Organic Electronics* 2010, 11, 1864.
149. Kim, K. K.;Reina, A.;Shi, Y.;Park, H.;Li, L.;Lee, Y. H.;Kong, J., *Nanotechnology* 2010, 21, 285205.
150. Yu, J. -S.;Kim, I.;Kim, J. -S.;Jo, J.;Larsen-Olsen, T. T.;Sondergaard, R. R.;Hosel M.;Angmo, D.;Jorgensen, M.;Krebs, F. C., *Nanoscale* 2012, 4, 6032.
151. Kang, M.;Kim, M.;Kim, J.;Guo, L. J., *Adv. Mater.* 2008, 20, 4408.
152. Na, S.;Park, D. -W.;Kim, S. -S.;Yang, S. -Y.;Lee, K.;Lee, M. -H., *Semicond. Sci. Technol.* 2012, 27, 125002.
153. Choi, S.;Potsavage, W. J. Jr.;Kippelen, B., *Optics Express* 18, S3, A462.
154. Kim, J.-Y.;Hwang, C.-R.;Jo, S.-H.;Jung, W.-G., *Appl. Phys. Lett.* 2011, 99, 233304.
155. Miller, M. S.;O’Kane, J. C.;Niec, A.;Carmichael, R. S.;Carmichael, T. B., *ACS Applied Materials & Interfaces* 2013, 5, 10165.
156. Choi, D. Y.;Kang, H. W.;Sung, H. J.;Kim, S. S., *Nanoscale* 2013, 5, 977.
157. Tyler, T. P.;Brock, R. E.;Karmel, H. J.;Marks, T. J.;Hersam, M. C., *Adv. Engy. Mater.* 2011, 1, 785.
158. Najeeb, C. K.;Lee, J.-H.;Chang, J.;Kim, J.-H., *Nanotechnology* 2010, 21, 385302.
159. Bedeloglu, A.;Jimenez, P.;Demir, A.;Bozkurt, Y.;Maser, W. K.;Sariciftci, N. S., *Journal of the Textile Institute* 2011, 102, 857.
160. Lin, C.-Y.;Kuo, D.-H.;Chen, W.-C.;Ma, M.-W.;Liou, G.-S., *Organic Electronics* 2012, 13, 2469.
161. Chaudhary, S.;Lu, H.;Mueller, A. M.;Bardeen, C. J.;Ozkan, M., *Nano Lett.* 2007, 7, 1973.
162. Cho, D.-Y.;Eun, K.;Choa, S.-H.;Kim, H.-K., *Carbon* 2014, 66, 530.
163. Tung, V. C.;Chen, L.-M.;Allen, M. J.;Wassei, J. K.;Nelson, K.;Kaner, R. B.;Yang, Y., *Nano Lett.* 2009, 5, 1949.
164. Li, C.;Li, Z.;Zhu, H.;Wang, K.;Wei, J.;Li, X.;Sun, P.;Zhang, H.;Wu, D., *J. Phys. Chem. C* 2010, 33, 14008.
165. King, P. J.;Khan, U.;Lotya, M.;De, S.;Coleman, J. N., *ACS Nano* 2010, 7, 4238.
166. Yu, K.;Lu, G.;Bo, Z.;Mao, S.;Chen, J., *J. Phys. Chem. Lett.* 2011, 13, 1556.
167. Chen, J.;Wen, Y.;Guo, Y.;Wu, B.;Huang, L.;Xue, Y.;Geng, D.;Wang, D.;Yu, G.;Liu, Y., *J. Am. Chem. Soc.* 2011, 44, 17548.
168. Tung, V. C.;Kim, J.;Huang, J., *Adv. Engy. Mater.* 2012, 2, 299.
169. Kim, J.;Tung, V. C.;Huang, J., *Adv. Engy. Mater.* 2011, 1, 1052.
170. Ahn, Y.;Jeong, Y.;Lee, Y., *ACS Applied Materials & Interfaces* 2012, 4, 6410.
171. Lee, M.-S.;Lee, K.;Kim, S.-Y.;Lee, H.;Park, J.;Choi, K.-H.;Kim, H.-K.;Kim, D.-G.;Lee, D.-Y.;Nam, S.;Park, J.-U., *Nano Lett.* 2013, 6, 2814.
172. Kim, S. M.;Walker, B.;Seo, J. H.;Kang, S. J., *Jpn. J. Appl. Phys.* 2013, 52, 125103.
173. Wang, J. T.-W.;Ball, J. M.;Barea, E. M.;Abate, A.;Alexander-Webber, J. A.;Huang, J.;Saliba, M.;Mora-Sero, I.;Bisquert, J.;Snaith, H. J.;Nicolas, R. J., *Nano Lett.* 2013, 131216131814005 DOI: 10.1021/nl403997a.
174. Wei, D.;Lu, Y.;Han, C.;Niu, T.;Chen, W.;Wee, A. T. S., *Angew. Chem., Int. Ed.* 2013, 52, 14121.
175. Zhang, L.;Shi, Z.;Wang, Y.;Yang, R.;Shi, D.;Zhang, G., *Nano Res.* 2011, 3, 315.
176. Hwang, J.;Kim, M.;Campbell, D.;Alsaman, H. A.;Kwak, J. Y.;Shivaraman, S.;Woll, A. R.;Singh, A. K.;Hennig, R. G.;Gorantla, S.;Rümmeli, M. H.;Spencer, M. G., *ACS Nano* 2012, 1, 385.
177. Barnes, T. M.;Bergeson, J. D.;Tenent, R. C.;Larsen, B. A.;Teeter, G.;Jones, K. M.;Blackburn, J. L.; van de Lagemaat, *J. Appl. Phys. Lett.* 2010, 96, 243309.

Biography

Dr. Yong Zhang is Global Market Segment Manager of Sigma-Aldrich Corp. He holds a Ph.D. in Chemical Engineering from the University of Rochester, and earned his M.B.A. from Kelley School of Business at Indiana University.

Dr. Bryce P. Nelson is Global Manager, Materials Science Product Management & R&D of Sigma-Aldrich Corp. He holds a Ph.D. in Chemistry from the University of Wisconsin-Madison.